SLAC-PUB-7571
June 1997

# PRODUCTION OF $\pi^{\pm}$, $K^{\pm}$, $K^0$, $K^{*0}$, $\phi$, p and $\Lambda^0$ IN HADRONIC $Z^0$ DECAYS

**The SLD Collaboration**[**]
Stanford Linear Accelerator Center
Stanford University, Stanford, CA 94309

## ABSTRACT

We have measured production rates as a function of momentum of the identified hadrons $\pi^+$, $K^+$, $K^0$, $K^{*0}$, $\phi$, p, $\Lambda^0$ and their antihadrons in inclusive hadronic $Z^0$ decays, as well as separately in decays into light, $c$ and $b$ flavors. In addition we have compared hadron and antihadron production rates in light quark (rather than anti-quark) jets. The SLD Cherenkov Ring Imaging Detector was used to identify charged hadrons. The vertex detector was used to tag high-purity samples of light- and $b$-flavor events. The electron beam polarization was used to tag samples of quark and antiquark jets. Clear flavor dependences are observed, consistent with expectations based upon measured production and decay properties of heavy hadrons. We use the light-flavor results to test the predictions of MLLA QCD and of various fragmentation models. Differences between hadron and antihadron production in light quark jets are observed at high momentum fraction, providing direct evidence that higher-momentum particles are more likely to contain a primary quark or antiquark, and we use these results to make a new direct measurement of strangeness suppression in the jet fragmentation process.

Contributed to the XVIII International Symposium on Lepton Photon Interactions, July 28 - August 1 1997, Hamburg, Germany, and to the International Europhysics Conference on High Energy Physics, 19-26 August 1997, Jerusalem, Israel; Ref: 287.

# 1 Introduction

The production of final state hadrons from primary hard partons, e.g. the quark and antiquark in $e^+e^- \to Z^0 \to q\bar{q}$, is currently believed to proceed in three stages. The first stage involves the radiation of gluons from the primary quark and antiquark, which in turn radiate gluons or split into $q\bar{q}$ pairs until their virtuality approaches the hadron mass scale. Such a "parton shower" is calculable in perturbative QCD, for example in the Modified Leading Logarithm Approximation (MLLA) [1].

The second stage, in which these partons turn into "primary" hadrons, is not understood quantitatively, although several hadronization models exist. A simple model is the ansatz of Local Parton-Hadron Duality (LPHD) [1], which hypothesizes that distributions of kinematic quantities for a given hadron species are directly proportional to the parton distributions at some appropriate parton virtuality. This allows the prediction via MLLA QCD of the shapes of differential cross sections for primary hadrons, and of, for example, the energy- and mass-dependences of the peak of the distribution of $\xi = -\ln(x_p)$, where $x_p = 2p/E_{cm}$, $p$ is the hadron momentum and $E_{cm}$ is the $e^+e^-$ center-of-mass energy.

The third stage, in which unstable primary hadrons decay into final state hadrons, complicates the interpretation of inclusive measurements. It is desirable to remove the effects of these decays when comparing with the predictions of QCD+LPHD. Additional complications arise in jets initiated by heavy ($c$ or $b$) quarks in which the leading heavy hadrons carry a large fraction of the beam energy, restricting that available to other primary particles, and then decay into a number of secondary particles. It is thus also desirable to restrict measurements to events with light primary flavors.

Measurements of the differential cross sections of identified particles are useful for testing the predictions of QCD+LPHD and constraining models. Several such measurements have been reported in $e^+e^-$ annihilation and QCD+LPHD has been successful in describing the shape and energy dependence of the $\xi$ distribution of inclusive charged particles, as well as those of identified charged and neutral hadrons [2]. At a given $E_{cm}$, the $\xi$ distribution for identified pions peaks at a higher value than the distributions for higher mass particle types; however little mass dependence is observed among these other species, although results for mesons and baryons are consistent with the hypothesis of separate mass dependences. It is probable that these peak positions, especially for pions, are influenced strongly by decay products of heavier particles; experimental elucidation of this issue is desirable.

A particularly interesting aspect of jet fragmentation is the question of what happens to the primary quark or antiquark that initiated the jet. Many fragmentation models assume that the initial quark is "contained" as a valence constituent of a particular hadron, and that this "leading" hadron has on average a higher momentum than the other particles in the jet. This phenomenon has not been studied in detail for high-energy light-flavor jets, since it is difficult to identify the sign and flavor of the initial $q/\bar{q}$ on a jet-by-jet basis. The establishment and quantification of leading

particle effects could lead to ways to identify the primary flavor of arbitrary samples of jets, enabling a number of new measurements in $e^+e^-$, as well as in $e$p and p$\bar{\text{p}}$, collisions.

In this paper we present an analysis of $\pi^\pm$, $K^\pm$, $K^0$, $K^{*0}/\bar{K}^{*0}$, $\phi$, p/$\bar{\text{p}}$, and $\Lambda^0/\bar{\Lambda}^0$ production in hadronic $Z^0$ decays collected by the SLC Large Detector (SLD). The analysis is based upon the approximately 150,000 hadronic events obtained in runs of the SLAC Linear Collider (SLC) between 1993 and 1995. We measure differential cross sections in an inclusive sample of hadronic events of all flavors, and also in high-purity samples of light- ($Z^0 \to u\bar{u}, d\bar{d}, s\bar{s}$) and $b$-flavor ($Z^0 \to b\bar{b}$) events. From these three samples we extract corrected differential cross sections in light- and $b$-, as well as $c$-flavor ($Z^0 \to c\bar{c}$) events. The unfolded differential cross sections for the light-flavor events are free from effects of heavy quark production and decay, and as such provide a more appropriate sample for comparison with QCD predictions, which generally assume massless quarks, although the influence of decay products of other unstable primary hadrons remains. We use these measurements to test the predictions of MLLA QCD+LPHD and of various fragmentation models.

We then select samples of quark and antiquark jets from our light-flavor event sample, using the large forward-backward production asymmetry in polar angle inherent in collisions of highly polarized electrons with positrons. The differential cross sections are measured separately for hadrons and antihadrons in light quark jets, and the observed differences are interpreted in terms of leading particle effects. In addition to new tests of fragmentation models, these measurements provide a new direct method [3] for measuring strangeness suppression in the fragmentation process at high $x_p$.

# 2 The SLD and Hadronic Event Selection

This analysis of data from the SLD [4] used charged tracks measured in the Central Drift Chamber (CDC) [5] and silicon Vertex Detector (VXD) [6]. The CDC consists of 80 layers of sense wires arranged in 10 axial or stereo superlayers in a uniform axial magnetic field of 0.6 T. The VXD is composed of CCDs containing a total of 120 million $22\times22$ $\mu$m pixels arranged in four concentric layers of radius between 2.9 and 4.2 cm. Including the uncertainty on the primary interaction point (IP), the CDC and VXD give a combined impact parameter resolution in the plane transverse to the beam axis of $11\oplus70/(p_\perp\sqrt{\sin\theta})$ $\mu$m, where $p_\perp$ is the track momentum transverse to the beam axis in GeV/c and $\theta$ is the polar angle of the tracks with respect to the beam axis.

Identification of charged particles is accomplished with the barrel portion of the SLD Cherenkov Ring Imaging Detector (CRID) [7], which covers the polar angle range $|\cos\theta| \leq 0.68$. Through the combined use of liquid $C_6F_{14}$ and gaseous $C_5F_{12}$ radiators, the CRID is designed to perform efficient charged $\pi$/K/p separation over most of the momentum range up to 45 GeV/c. A charged particle that passes through a radiator of refractive index $n$ with velocity above Cherenkov threshold, $\beta > \beta_0 = 1/n$, emits

photons at an angle $\theta_c = \cos^{-1}(1/\beta n)$ with respect to its flight direction. Such photons are imaged through quartz windows into time projection chambers (TPCs) containing a photosensitive gas. The resulting photoelectrons drift to wire chambers where the conversion point of each is measured in three dimensions using drift time, wire address and charge division. These positions are used to reconstruct a Cherenkov angle with respect to each extrapolated charged track. We discuss the performance of the CRID in the following sections.

The trigger and initial selection of hadronic events is described in [8]. The analysis presented here is based on charged tracks measured in the CDC and VXD. A set of cuts was applied in order to select events well-contained within the detector acceptance. Tracks were required to have (i) a closest approach to the beam axis within 5 cm, and within 10 cm along the beam axis of the measured interaction point (IP), (ii) a polar angle $\theta$ with respect to the beam axis with $|\cos\theta| < 0.80$, (iii) a momentum transverse to this axis $p_\perp > 150$ MeV/$c$, and (iv) a momentum $p < 50$ GeV/c. Events were required to contain a minimum of seven such tracks, to have a thrust [9] axis polar angle with respect to the beam axis $\theta_T$ within $|\cos\theta_T| < 0.71$, to contain a minimum charged visible energy $E_{vis} > 18$ GeV, where all tracks were assigned the charged pion mass, and to have good VXD data [10] and a well-measured IP position. A sample of about 90,000 events passed these cuts.

Samples of events enriched in light and $b$ primary flavors were selected based on charged track impact parameters $\delta$ with respect to the IP in the plane transverse to the beam [11]. For each event we define $n_{sig}$ as the number of tracks with impact parameter greater than three times its estimated error, $\delta > 3\sigma_\delta$. Events with $n_{sig} = 0$ were assigned to the light flavor sample and those with $n_{sig} \geq 3$ were assigned to the $b$ sample. The light and $b$ samples comprised roughly 60,000 and 14,500 events, with purities of 86% and 90%, respectively, estimated from our Monte Carlo simulation.

Separate samples of hemispheres enriched in light-quark and light-antiquark jets were selected from the light-tagged event sample by exploiting the large electroweak forward-backward production asymmetry wrt the beam direction. The event thrust axis was used to approximate the initial $q\bar{q}$ axis and was signed such that its $z$-component was positive, $\hat{t}_z > 0$. Events in the central region of the detector, where the production asymmetry is small, were removed by the requirement $|\hat{t}_z| > 0.2$, leaving 35,473 events. The quark-tagged hemisphere in events with left-(right-)handed electron beam was defined to comprise the set of tracks with positive (negative) momentum projection along the signed thrust axis. The remaining tracks in each event were defined to be in the antiquark-tagged hemisphere. The sign and magnitude of the electron beam polarization were measured for every event. For the selected event sample, the average magnitude of the polarization was 0.73. Using this value and assuming Standard Model couplings, the tree-level purity of the quark-tagged sample is 0.73.

# 3 CRID Performance

Here we note the performance parameters of the CRID relevant to this analysis. The liquid (gas) radiator index of refraction was measured to be 1.282 (1.00172), corresponding to $\pi/K/\mathrm{p}$ thresholds of 0.17/0.62/1.17 (2.4/8.4/16.0) GeV/c. The gas index was tracked with an online SONAR monitor and time variations of up to $\pm 0.0001$ were found and corrected. The average detected photon yield was 12.8 (9.2) per full ring for tracks with high velocity in hadronic events. The average Cherenkov angle resolution was 16 (4.5) mrad including the effects of residual misalignments and track extrapolation resolution. The local or intrinsic resolution was 13 (3.8) mrad, consistent with the design value.

Tracks were identified using a likelihood technique [12]. For each of the three charged hadron hypotheses $i = \pi, K$, p, a likelihood $L_i$ was calculated based upon the number of detected photoelectrons and their measured angles, the expected number of photons, the expected Cherenkov angle and a background term. The background included the effects of overlapping Cherenkov radiation from other tracks in the event as well as a constant term normalized to the number of unassociated hits in the TPC in question. Particle separation was based upon differences between logarithms of these three likelihoods, $\mathcal{L}_i = \ln L_i$. The particle identification performance of the barrel CRID depends on the track selection for a given analysis, and is discussed where relevant in the following sections.

# 4 Charged Hadron Fractions

In this section we describe the production measurements of charged pions, kaons and protons, which were identified using the CRID. Information from the liquid (gas) radiator only was used for tracks with $p < 2.5$ ($p > 7.5$) GeV/c; in the overlap region, $2.5 < p < 7.5$ GeV/c, liquid and gas information was combined. Additional track selection cuts were applied to remove tracks that scattered through large angles before exiting the CRID and to ensure that the CRID performance was well-modelled by the simulation. Tracks were required to have at least 40 CDC hits, at least one of which was in the outermost superlayer, to extrapolate through an active region of the appropriate radiator(s), and to have at least 80 (100)% of their expected liquid (gas) ring contained within a sensitive region of the CRID TPCs. The latter requirement included rejection of tracks with $p > 2.5$ GeV/c for which there was a saturated CRID hit (from passage of miminum-ionizing particles) within a 5 cm radius (twice the maximum ring radius) of the expected gas ring center. Tracks with $p < 7.5$ GeV/c were required to have a saturated hit within 1 cm of the extrapolated track, and tracks with $p > 2.5$ GeV/c were required to have either such a saturated hit or the presence of at least four hits consistent with a liquid ring. These cuts accepted 47, 28 and 43% of tracks within the barrel acceptance in the momentum ranges $p < 2.5$, $2.5 < p < 7.5$ and $p > 7.5$

GeV/c, respectively. For momenta below 2 GeV/c, only negatively charged tracks were used to reduce the background from protons produced in interactions with the detector material.

For tracks with $p < 2.5$ ($p > 2.5$) GeV/c, we define a particle to be identified as type $j$, where $j = \pi, K$,p, if $\mathcal{L}_j$ exceeds both of the other log-likelihoods by at least 5 (3) units. Efficiencies for identifying selected particles of true type $i$ as type $j$ were determined where possible from the data. A detailed Monte Carlo (MC) simulation of the detector was then used to make small corrections to these measurements, and to derive the remaining efficiencies from those measured [13]. Tracks from selected $K_s^0$ and $\tau$ decays in the data were used as "pion" test samples, having estimated non-$e/\mu/\pi$ contents of 0.3 and 1.7% respectively. Figure 1 shows the probability for these tracks to be identified as (a) pions, (b) kaons and (c) protons. Also shown are results of the same analysis of corresponding MC samples. The MC describes the momentum dependence very well and reproduces the efficiencies to within $\pm 0.03$. Functional forms were chosen that described the momentum dependence of both data and simulated test samples as well as that of simulated true pions in hadronic events, and fitted to the data. The simulation was used to correct the fitted parameters for non-pion content in the $K_s^0$ and $\tau$ samples and differences in tracking performance between tracks in these samples and those in hadronic events. The resulting identification efficiency functions are shown in the leftmost column of fig. 2.

A similar procedure using only $\pi$ and p likelihoods was used to measure the $\pi$-p separation in the liquid (gas) system for $p > 2$ (17) GeV/c, and the simulation was used to derive from that the p$\rightarrow$p identification efficiency in these momentum ranges, shown in the bottom right of fig. 2. The remaining p$\rightarrow$p efficiencies, as well as the $\pi$-$K$ separation in the gas system below and near kaon threshold ($p < 10$ GeV/c), were measured using protons from $\Lambda^0$ decays [13]. The remaining efficiencies in fig. 2 were derived from the measured ones using the simulation. For example, the $K \rightarrow K$ efficiency is equal to the $\pi \rightarrow \pi$ efficiency for momenta in the ranges $1.5 < p < 2.5$ and $15 < p < 25$ GeV/c, since both particles are well above the relevant Cherenkov threshold and their expected Cherenkov angles differ from that of the proton by an amount large compared with the angular resolution. Just below these ranges the $\pi \rightarrow \pi$ efficiency was scaled by a rising exponential to account for the effect of the reduced photon yield near kaon threshold. Above the upper range it was scaled by a Gaussian falloff to account for the fact that the expected kaon ring radius is between those of pions and protons.

The pairs of lines shown in fig. 2 represent our estimated efficiencies plus and minus their systematic uncertainties. For the diagonal entries, these uncertainties correspond to errors on the fitted parameters and are completely positively correlated across each of the three momentum regions. For the off-diagonal terms, representing misidentification rates, a more conservative 25% relative error was assigned at all points to account for the limited experimental constraints on the momentum dependence. These errors are also strongly positively correlated among momenta.

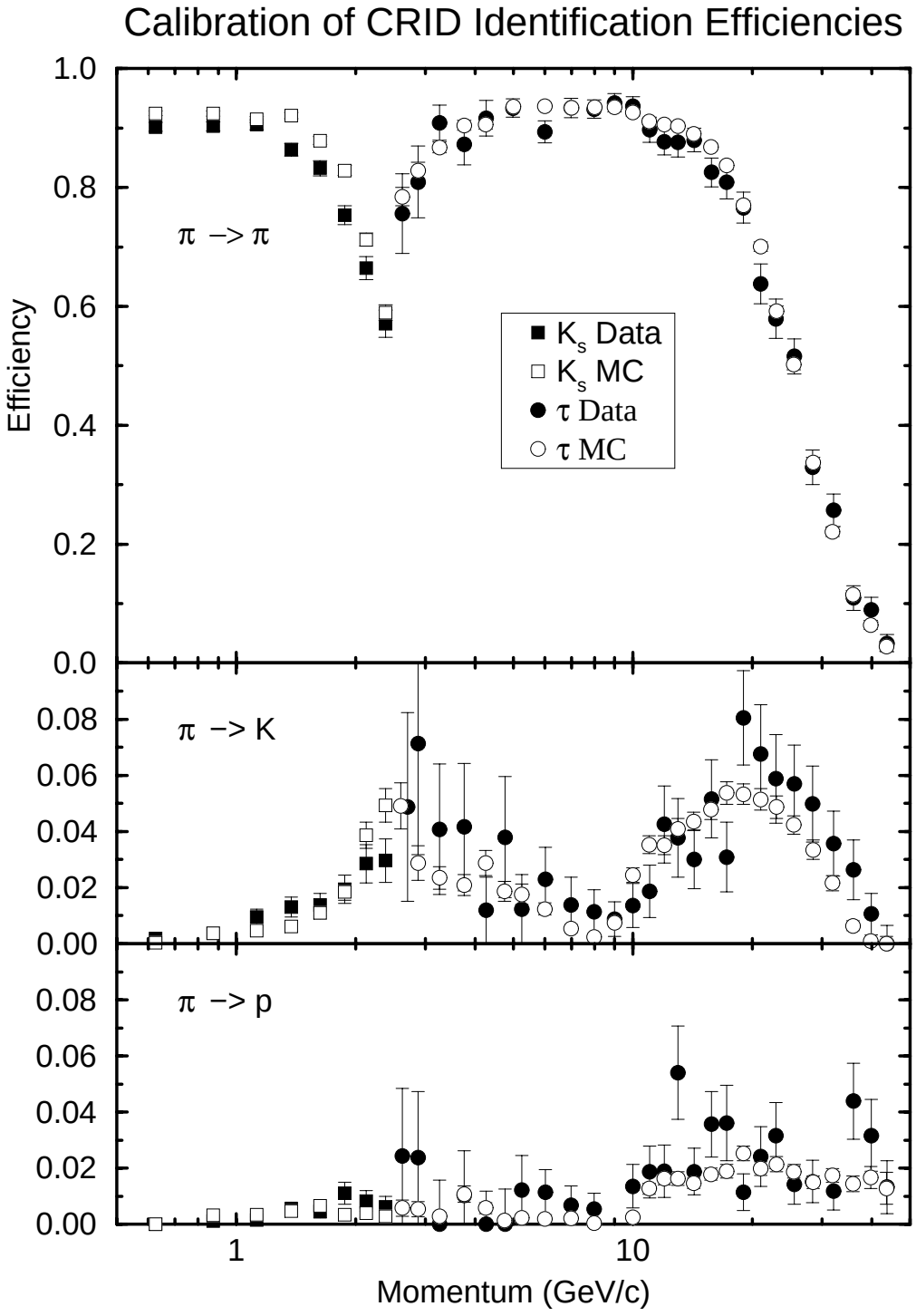


Figure 1: Efficiencies for selected tracks from $K_s^0$ (squares) and $\tau$ (circles) decays to be identified as each hadron type in the CRID. The solid symbols represent the data and the open symbols the simulation

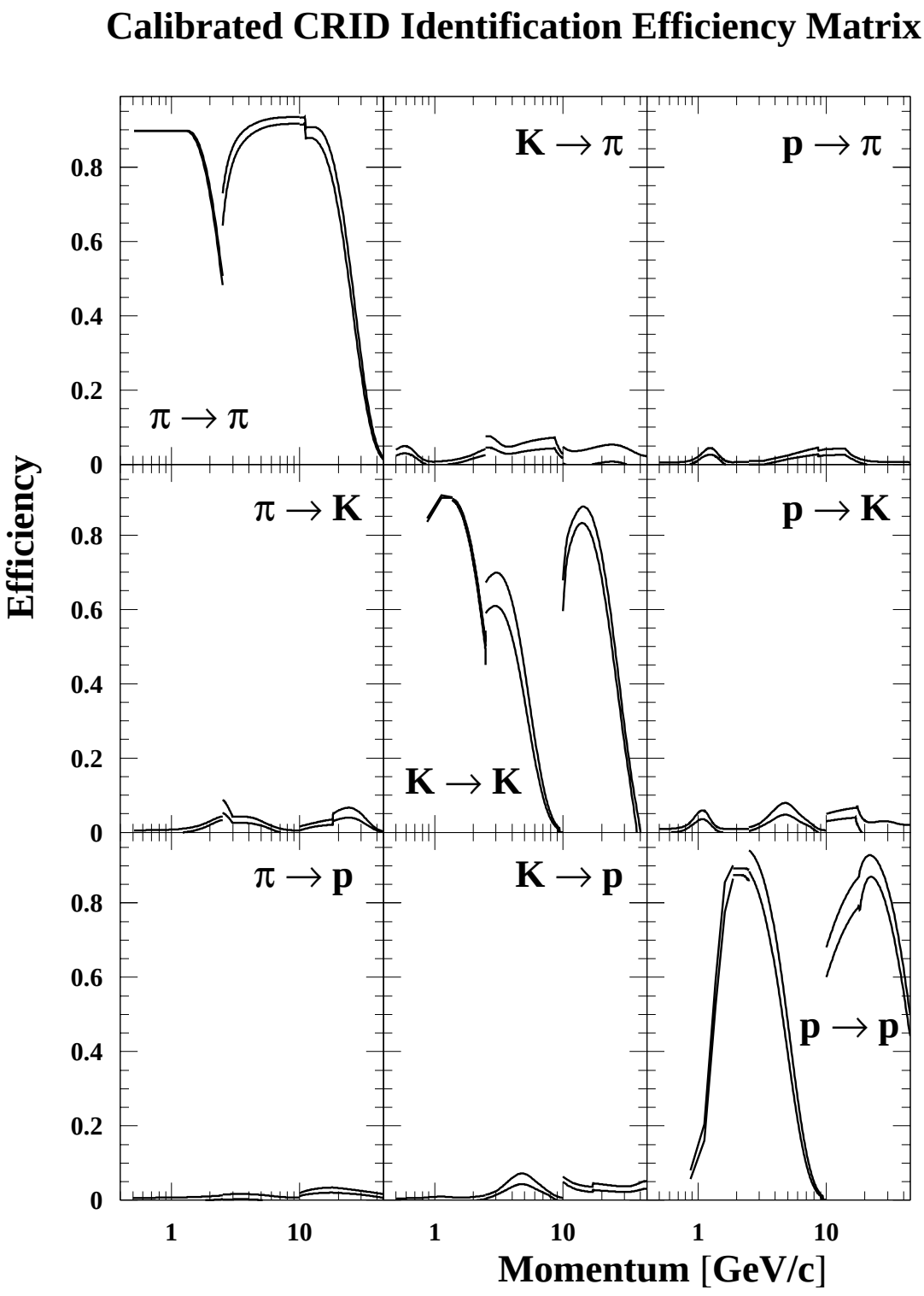


Figure 2: Calibrated identification efficiencies for tracks used in the charged hadron fractions analysis. The separations between the pairs of lines represent the systematic uncertainties, which are strongly correlated between momenta.

The identification efficiencies in fig. 2 peak near or above 0.9 and the pion coverage is continuous from 0.5 GeV/c up to approximately 35 GeV/c. There is a gap in the kaon-proton separation between 7 and 10 GeV/c due to limited resolution of the liquid system and the fact that both particles are below Cherenkov threshold in the gas system. The proton coverage extends to the beam momentum. Misidentification rates are typically less than 0.03, with peak values of up to 0.07.

In each momentum bin we measured the fractions of the selected tracks that were identified as $\pi$, $K$ and p. The observed fractions were related to the true production fractions by an efficiency matrix, composed of the values in fig. 2 for that bin. This matrix was inverted and used to unfold our observed identified particle rates. This analysis procedure does not require that the sum of the charged particle fractions be unity; instead the sum was used as a consistency check and was found to be within statistical errors of unity for all momenta. In some momentum regions we cannot distinguish two of the three species, so the procedure was reduced to a $2\times2$ matrix analysis and we present only the fraction of the identified species, i.e. protons above 35 GeV/c and pions between 6 and 9.5 GeV/c.

Electrons and muons were not distinguished from pions in this analysis; this background was estimated from the simulation to be about 5% in the inclusive flavor sample, predominantly from $c$- and $b$-flavor events. The flavor-inclusive fractions were corrected using the simulation for the lepton backgrounds, as well as for the effects of beam-related backgrounds, particles interacting in the detector material, and particles with large flight distance, such that the conventional definition of a final-state charged hadron is recovered, namely charged pions, kaons or protons that are either from the primary interaction or decay products of particles with lifetime less than $3\times10^{-10}$s.

The measured charged particle fractions for inclusive hadronic $Z^0$ decays are shown in fig. 3. The errors on the points below 15 GeV/c are dominated by the systematic uncertainties on the identification efficiencies and are strongly positively correlated across the entire momentum range. For $p > 15$ GeV/c the errors have roughly equal statistical and systematic contributions, and the systematic errors are positively correlated and increase in magnitude with momentum.

Pions are seen to dominate the charged hadron production at low momentum, and to decline steadily in fraction as momentum increases. The kaon fraction rises steadily to about one-third at high momentum. The proton fraction rises to a maximum of about one-tenth at about 10 GeV/c, then declines slowly. Where the momentum coverage overlaps, these measured fractions were found to be in agreement with previous measurements at the $Z^0$ [14, 15, 16]. Measurements based on ring imaging and those based on ionization energy loss rates [15, 16] cover complementary momentum ranges and can be combined to provide continuous coverage over the range $0.2 < p < 35$ GeV/c. Differential production cross-sections were obtained by multiplying these fractions by the inclusive charged hadron differential cross section generated by the JETSET 7.4 [17] simulation program, which provides a good description of inclusive charged particle distributions at the $Z^0$ [18].

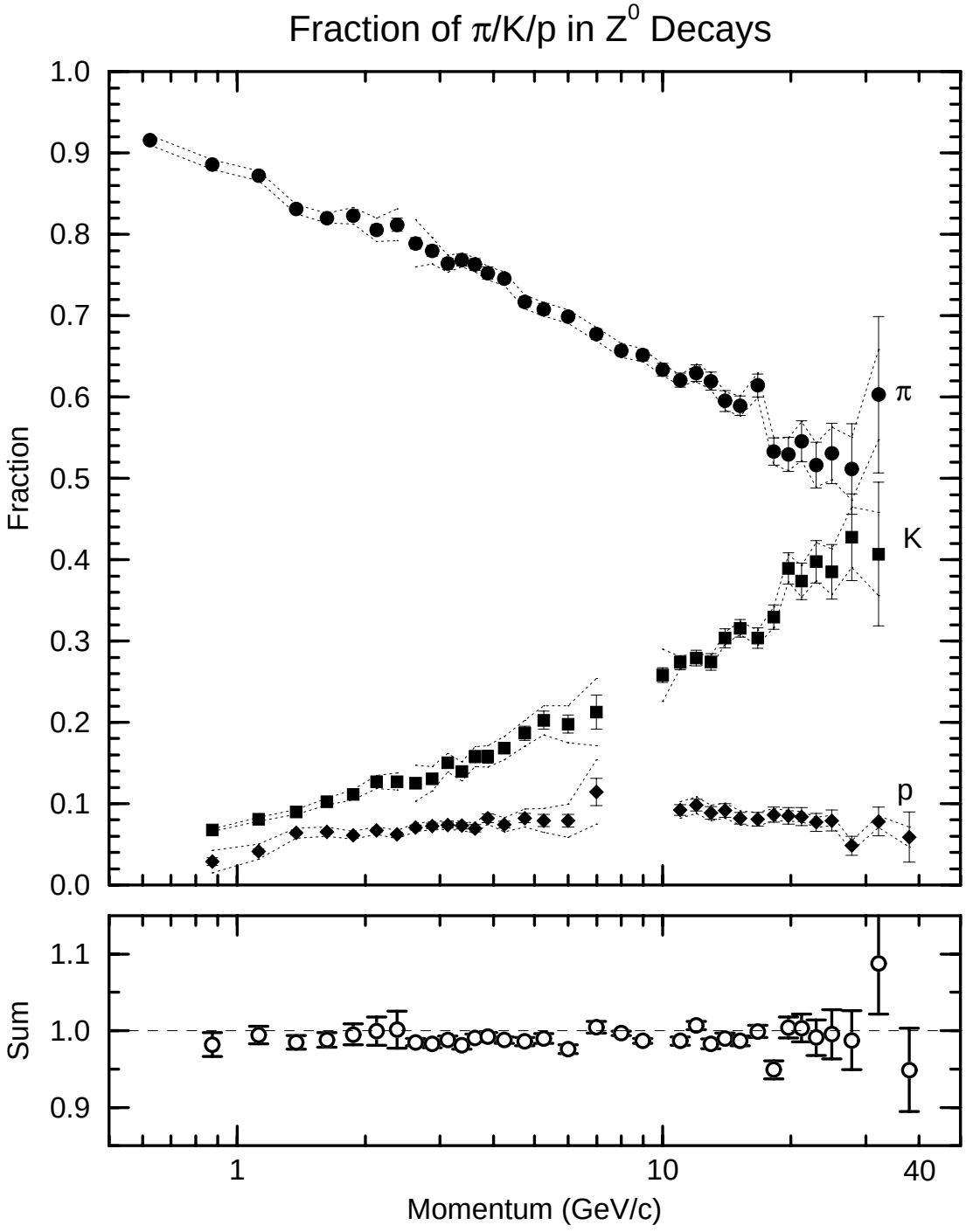


Figure 3: Measured charged hadron production fractions in hadronic $Z^0$ decays. The circles represent the $\pi^{\pm}$ fraction, the squares the $K^{\pm}$ fraction, the diamonds the $\mathrm{p}/\bar{\mathrm{p}}$ fraction, and the open circles the sum of the three fractions. The error bars are statistical only. The dotted lines indicate the systematic errors, which are strongly correlated between momenta (see text).

# 5 Neutral $K^0$ and $\Lambda^0/\bar{\Lambda}^0$ Production

In this section we describe the production measurements [19] of $K^0$ and $\Lambda^0/\bar{\Lambda}^0$. We reconstructed the charged decay modes $K_s^0 \to \pi^+\pi^-$ and $\Lambda^0(\bar{\Lambda}^0) \to \mathrm{p}(\bar{\mathrm{p}})\pi^{\mp}$, collectively referred to as $V^0$ decays. Track selection cuts were applied in order to ensure good invariant mass resolution. We required: a minimum transverse momentum of 150 MeV/c with respect to the beam direction; at least 40 hits measured in the CDC; and a polar angle satisfying $|\cos\theta| < 0.8$.

Pairs of oppositely charged tracks satisfying these requirements were then combined to form $V^0$s if their separation was less than 15 mm at their point of closest approach in 3 dimensions. A $\chi^2$ fit of the two tracks to a common vertex was performed, and to reject combinatoric background we required: the fit probability of the two tracks to a common vertex to be greater than 2%; this secondary vertex to be separated from the IP by at least 1 mm, and by at least $5\sigma_l$, where $\sigma_l$ is the calculated error on the separation length of the $V^0$; and secondary vertices reconstructed outside the Vertex Detector to have fewer than two VXD hits assigned to each track.

Two invariant masses were then calculated for each pair using the momenta of the charged tracks at the fitted vertex position. The charged pion mass was assigned to both tracks to give $m_{\pi\pi}$, and the proton (pion) mass was assigned to the higher-(lower)-momentum track to give $m_{p\pi}$. In the plane perpendicular to the beam, the angle between the vector sum of the momenta of the two charged tracks and the line joining the IP to the secondary vertex was required to be less than both 60 mrad and $k \cdot (2 + 20/p_T + 5/p_T^2)$ mrad. Here, $p_T$ is the component of the vector sum momentum transverse to the beam in units of GeV/c and $k$=1.75 for $\Lambda^0/\bar{\Lambda}^0$ candidates and 2.5 for $K_s^0$ candidates. For $\Lambda^0/\bar{\Lambda}^0$ candidates, a minimum vector-sum momentum of 500 MeV/c was required.

Note that it is possible at this stage for one $V^0$ to be considered a candidate for both the $K_s^0$ and $\Lambda^0/\bar{\Lambda}^0$ hypotheses. Kinematic regions exist where the two hypotheses cannot be distinguished without particle identification. In addition there is background from other processes that occur away from the IP, most notably $\gamma$-conversions into $e^+e^-$ pairs. Depending upon the type of analysis, such "kinematic-overlaps" may introduce important biases. In this analysis, the kinematic-overlap region was removed only when it distorted the relevant invariant mass distribution. For the $K_s^0$ analysis, the $\Lambda^0/\bar{\Lambda}^0$ background causes an asymmetric bump in the $\pi\pi$-invariant mass distribution, which complicated the subsequent fitting procedure. A cut on the $\pi^+$ helicity angle $\theta_\pi^*$, defined as the angle between the $\pi^+$ momentum vector in the $K_s^0$ rest frame and the $K_s^0$ flight direction, of $|\cos\theta^*| \leq 0.8$ was used to remove the $\Lambda^0$ and $\bar{\Lambda}^0$ contamination, as well as that from $\gamma$-conversions.

For the $\Lambda^0/\bar{\Lambda}^0$ analysis, the shape of the $K_s^0$ background depends on momentum. Above a $V^0$ momentum of a few GeV/c, the $K_s^0 \to \pi^+\pi^-$ background is essentially uniform in the peak region of the p$\pi$ invariant-mass distribution and no cuts were made to remove the $K_s^0$ overlap. At sufficiently low momentum, the $K_s^0$ background

becomes asymmetric under the $\Lambda^0/\bar{\Lambda}^0$ peak due to detector acceptance; the softer $\pi$ fails to be reconstructed and thus the $K_s^0$ is not found. Therefore, $\Lambda^0/\bar{\Lambda}^0$ candidates with total momentum below 1.8 $GeV/c$ were required to have $m_{\pi\pi}$ more than $3\sigma$ away from the $K_s^0$ mass, where $\sigma$ is the measured resolution on $m_{\pi\pi}$, parameterized as $\sigma_{\pi\pi}(p) = 4.6 - .27p + .21p^2 - .01p^3$ MeV/c$^2$. In order to remove $\gamma$ conversions, the proton helicity angle was required to satisfy $\cos\theta^*_{\rm p} \geq -0.95$.

The $V^0$ candidates were binned in scaled momentum, $x_p$, and the resulting invariant mass distributions were then fitted. The nominal shape used for the signal mass peak was a sum of two Gaussians of common center, whose relative fractions and nominal widths were fixed from the MC simulation. The normalization, common center, and a resolution scale-factor were free parameters of the fit. In most cases, a single Gaussian did not give an adequate description of the signal peak, since the mass resolution is momentum-dependent and varies substantially over the width of a typical scaled momentum bin. In some cases a sum of three Gaussians was needed. The nominal background shape used for the $K_s^0$ fits was a quadratic; for the $\Lambda^0$ fits a more complicated function was required due to the proximity of the kinematic edge to the signal peak. The function, $P_{bkg}(m) = a + b(m - m_0) + c(1 - e^{d((m-m_0)-0.038)})$ was found to be adequate in MC studies. In each bin, the $m_{\rm p\pi}$ and $m_{\pi\pi}$ distributions were fitted using the sum of the signal and background shapes. Sample fits for various momentum bins are shown in fig. 4.

The Efficiencies for reconstructing true $K_s^0$ and $\Lambda^0/\bar{\Lambda}^0$ decays were calculated, using the simulation, by repeating the full selection and analysis on the simulated sample and dividing by the number of generated $K_s^0$ or $\Lambda^0/\bar{\Lambda}^0$. Several checks were performed to verify the MC simulation, and thus the $V^0$ reconstruction efficiency. In particular, the lifetimes of the $K_s^0$ and $\Lambda^0$ were measured by binning the data in proper time rather than scaled momentum, yielding values consistent with the respective world averages. Two important discrepancies were found. There was a 2.7% excess in the average number of reconstructed tracks per event in the simulation with respect to the data both before and after the track quality cuts were applied. Since the MC was tuned using the world-average measured charged multiplicity in hadronic $Z^0$ decays, we ascribe the difference to mismodelling of the overall track reconstruction efficiency. There was also a difference in the distribution of radial distances of reconstructed $V^0$ vertices from the beam between the data and the MC, the data showing a larger dip near a radius of 2 cm, just inside the inner layer of the vertex detector. We ascribe this to mismodelling of the linking of VXD hits to measured tracks from $V^0$ decays in this region. To correct for these two problems, tracks were removed randomly from the simulated events, as were $V^0$ candidates decaying in the appropriate radial range.

After these corrections were applied, the simulated reconstruction efficiencies were parametrized as functions of momentum, and are shown in fig. 5. These curves show three main features: 1) the reconstruction efficiency is limited by the detector acceptance of $\sim$0.67 and the charged decay branching fractions of 0.64 for $\Lambda^0/\bar{\Lambda}^0$ and 0.68 for $K_s^0$; 2) the efficiency at high momentum decreases due to finite detector size and two-

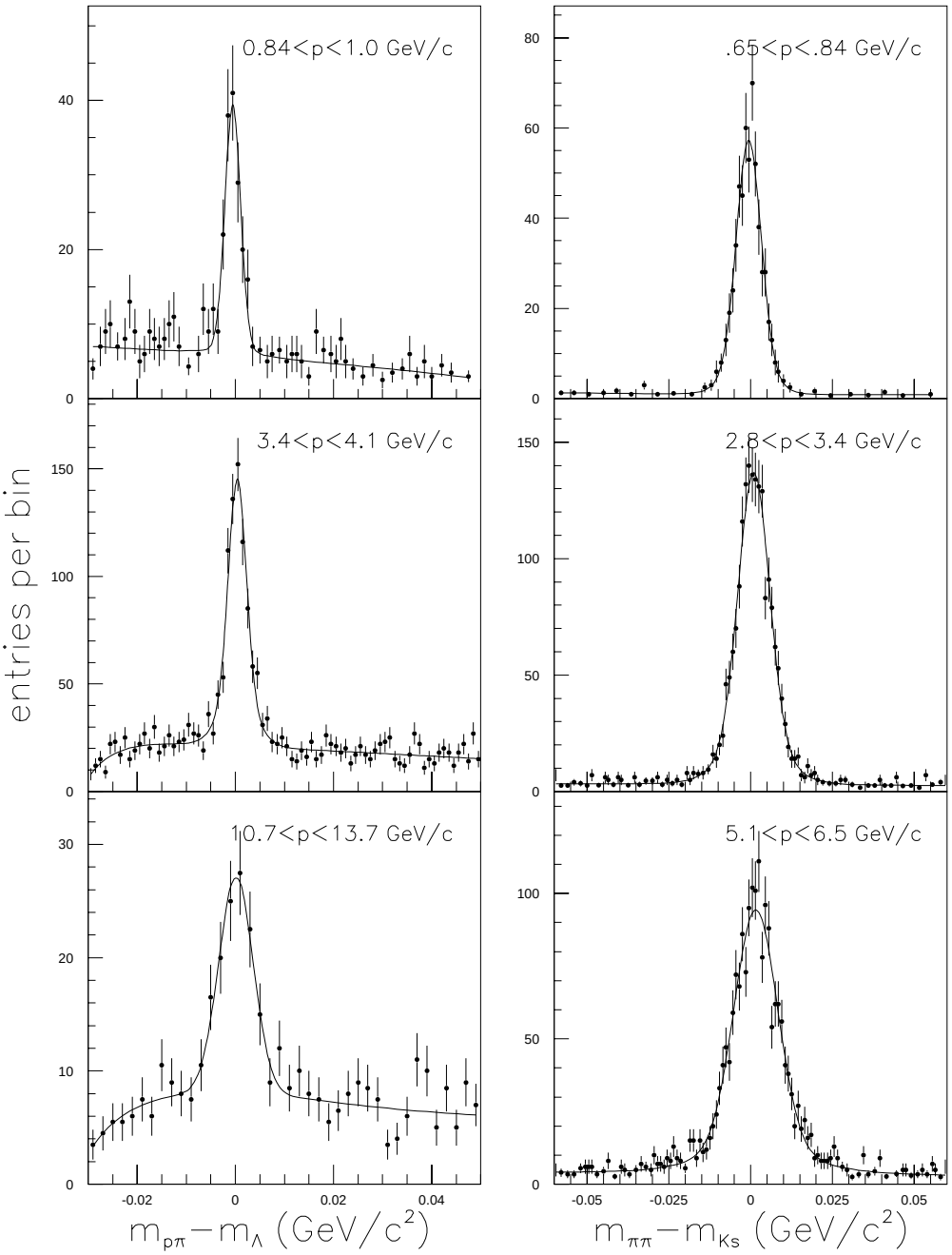


Figure 4: Sample invariant mass peaks from the data for $\Lambda^0(\bar{\Lambda}^0) \to p(\bar{p})\pi$ (left column) and $K_s^0 \to \pi^+\pi^-$ (right column) for low, medium, and high momentum bins. The points with error bars represent the data, and the lines represent the results of the fits described in the text.

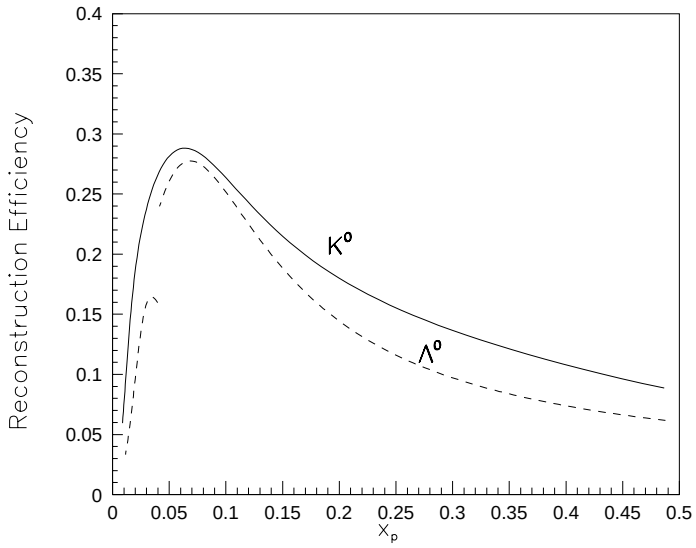


Figure 5: The parametrized simulated reconstruction efficiencies as a function of scaled momentum for $K_s^0$ (solid line) and $\Lambda^0/\bar{\Lambda}^0$ (dashed line). The charged decay branching ratios are included in the efficiency. Note the discontinuity in the $\Lambda^0/\bar{\Lambda}^0$ reconstruction efficiency; this is due to the invariant-mass cut to remove low momentum $K_s^0$ background.

track detector resolution; 3) the efficiency at low-momentum is limited by minimum $p_T$ and flight distance requirements. The discontinuity in the $\Lambda^0/\bar{\Lambda}^0$ reconstruction efficiency is due to the imposed $K_s^0$ mass cut for low-$x_p$ candidates.

The inclusive cross section $1/\sigma_{tot}\, d\sigma/dx_p$ was then calculated from the number of particles observed in each scaled- momentum bin:

$$\frac{1}{\sigma_{tot}}\frac{d\sigma}{dx_p} = \frac{1}{\mathcal{R}(x_p)}\frac{1}{\Delta x_p}\frac{N_{obs}(x_p)}{N_{recon}^{events}} \tag{1}$$

where $\sigma_{tot}$ is the total hadronic cross-section, $N_{obs}$ is the integrated area under the fitted mass peak, and $\Delta x_p$ is the bin width. As is conventional, the $K^0$ cross section was obtained by multiplying the measured $K_s^0$ cross section by a factor of 2 to account for the undetected $K_L^0$ component. The resulting differential cross sections, including point-to-point systematic errors, discussed below, are shown in fig. 9.

Four categories of systematic uncertainty were investigated for the $K_s^0$ and $\Lambda^0/\bar{\Lambda}^0$, analysis. An important contribution to the overall $V^0$ spectrum is the track reconstruction efficiency of the detector. As noted above the efficiency has been tuned using the world average measured charged multiplicity in hadronic $Z^0$ decays. We take a reasonable error of $\pm 1.7\%$ [20] on the world average multiplicity as the uncertainty on our reconstruction efficiency, which corresponds to a *normalization* error on the $K^0$

and $\Lambda^0/\bar{\Lambda}^0$ production rates of 3.4%. This uncertainty is independent of momentum and is not shown in any of the figures. A conservative 50% variation on the fraction of $V^0$ removed from the simulated events was used to estimate a systematic uncertainty due to remaining detector effects.

Each of the cuts used to select $V^0$ candidates was varied independently and the analysis repeated. For each bin the *rms* of this set of measurements was calculated and assigned as the systematic uncertainty due to modelling of the acceptance.

For both the $K^0$ and the $\Lambda^0/\bar{\Lambda}^0$ candidates, the signal and background shapes used in the fits were varied. Single and multiple independent Gaussians, without common centers or fixed widths, were used for the signal. Alternative background shapes included constants and polynomials of differing orders. In each case the fits were repeated on both data and simulated invariant mass distributions and the *rms* was assigned as a systematic uncertainty.

The MC statistical error for each bin in the reconstruction efficiency computation was also assigned as a systematic error.

# 6 Neutral $K^{*0}$ and $\phi$ Production

In this section we present the production measurements [21] for the neutral strange mesons $\phi$ and $K^{*0}$. We reconstruct the charged decay modes $\phi \to K^+K^-$ and $K^{*0}/\bar{K}^{*0} \to K^{\pm}\pi^{\mp}$. Additional track selection cuts were applied in order to ensure good invariant mass resolution: at least 40 hits measured in the CDC; a track fit quality of $\chi^2/\mathrm{dof} < 7$; and a polar angle satisfying $|\cos\theta| < 0.8$.

Pairs of oppositely charged tracks satisfying these requirements were then combined to form neutral candidates if a $\chi^2$ fit of the two tracks to a common vertex was successful. The background from long-lived species was rejected based upon the flight distance and vertex quality of the pair, and the accuracy by which the vector sum points back to the IP. The background from $\gamma$-conversions was rejected by assigning the electron mass to both tracks and requiring $m_{ee}$ to be greater than 70 MeV/$c^2$.

To reject the high combinatoric background from $\pi^+\pi^-$ pairs we used the CRID to identify charged kaon candidate tracks. Only liquid (gas) information was used for tracks with $p < 2.5\,(> 3.5)$ GeV/c, and liquid and gas information was combined for the remaining tracks. For this analysis a track was considered "identifiable" if it extrapolated through an active region of the appropriate CRID radiator(s); it was considered identified as a kaon if the log-likelihood difference between the kaon and pion hypotheses $\mathcal{L}_K - \mathcal{L}_\pi > 3$. These cuts are considerably looser than those in section 4, in order to maximize the acceptance for the neutral vector mesons. Efficiencies for identifying selected tracks as kaons by this definition were calibrated using data in a manner similar to that described in section 4. The $K \to K$ efficiency was found to have a momentum dependence very similar to the $\pi \to \pi$ efficiency shown in the upper left plot of fig. 2, with about 12% lower amplitude. There is no dip in the 3–10 GeV/c

region since no cut is made against protons. The $\pi \rightarrow K$ misidentification rate averages 10% and is roughly independent of momentum, however the exact value is unimportant for this analysis. The p$\rightarrow K$ misidentification rate is substantial, especially in the 3–10 GeV/c region, but protons constitute only a small part of the combinatoric background and again the exact value is unimportant.

A track pair was accepted as a $\phi \rightarrow K^+K^-$ candidate if both tracks were identified as kaons. A pair was accepted as a $K^{*0} \rightarrow K^+\pi^-$ candidate if one track was identified as a kaon and the other was not. The two samples are thus exclusive.

The $\phi$ candidates were binned in scaled momentum $x_p$, and the resulting $KK$-invariant mass distributions were fitted in a manner similar to that described above for the $V^0$ candidates. The nominal signal shape was a sum of Gaussians of common center; the area and a resolution scale-factor were free parameters, and the center was fixed at the PDG value [22]. The background shape was parametrized as a threshold term multiplied by a slowly decreasing exponential:

$$P_{bkg}(x) = N x^{\gamma} e^{c_1 x + c_2 x^2 + c_3 x^3 + c_4 x^4 + c_5 x^5} \tag{2}$$

where $x = m - 2m_K$, $N$ is an overall normalisation factor, and $\gamma$ and $c_{1\ldots5}$ are free parameters. The background parameters were first determined from fits to the $m_{KK}$ distributions of simulated true combinatorial background, as well as same-sign track pairs in the data, which were found to agree with each other and to describe the shape of the data distribution away from the signal peak. The parameters were then allowed to float within 20% of these values in the fit. The measured $m_{KK}$ distributions for the six $x_p$ bins are shown in fig. 6, along with the results of the fits.

The case of the $K^{*0}$ is considerably more complicated due to the natural width of the $K^{*0}$ and the presence of many reflections of resonances decaying into $\pi^+\pi^-(\pi^0)$. The $K^{*0}$ signal was parametrised using a relativistic Breit-Wigner with the amplitude free and the center and width fixed to PDG values [22]. The background was divided into combinatoric and resonant pieces. The combinatorial piece was described by a parametrisation similar to that of the $\phi$ but with seven polynomial parameters. Parameters derived from fits to simulated combinatoric background and a same-sign data test sample were found not to agree with each other or with the opposite-sign data away from the peak, and a search over a space of initial values was required in order to find the best fit.

Knowledge of the resonant contributions to the background is essential, since the $K^{*0}$ is a wide state and non-monotonic background variation within its width can lead to systematic errors in the measured rate. We considered four classes of reflections:

- $\rho^0 \rightarrow \pi^+\pi^-$, $K^0_s \rightarrow \pi^+\pi^-$, and $\omega^0, \eta, \eta' \rightarrow N\pi$, where one of the charged pions is misidentified as a $K^{\pm}$. These backgrounds are large, even after reduction by a factor of about 5 by the particle identification. They are particularly important since the combination of $\rho$ and $\omega$ decays gives rise to a dip in the total background near the center of the signal peak, and there is some uncertainty as to the shape of the $\rho$ resonance in $Z^0$ decays.

- $\gamma$ conversions where one electron is misidentified as a kaon. The other track is not actually misidentified, as no attempt is made to separate electrons from pions. These are removed effectively by the cut against $\gamma$ conversions noted above.

- $\phi \rightarrow K^+K^-$, where one track is misidentified as a pion. This background is reduced substantially by the requirement that only one of the tracks in the pair is identified as a kaon.

- $\Lambda \rightarrow p\pi$, where the proton is misidentified as a kaon. These are removed effectively by the cut against long-lived $V^0$ noted above. This and the last two categories give rise to a more pronounced shoulder in the background just below the signal peak, so their removal is quite useful in obtaining a robust fit.

The shape of the $m_{K\pi}$ distribution for each reflection was determined from the simulation, in which their production rates were set to world average values [22]. A scale factor for each category was included as a free parameter in the fit to account for possible mismodelling of the misidentification rates. Their fitted values were consistent with unity. Figure 7 shows the $m_{K\pi}$ distribution for each scaled momentum bin, along with the results of the fits.

As for the $K^0_s$ and $\Lambda^0/\bar{\Lambda}^0$ analysis, the $\phi$ and $K^{*0}/\bar{K}^{*0}$ reconstruction efficiencies were determined using the simulation. Corrections to the simulation were made for the tracking efficiency (see above) as well as for the efficiencies for tracks to be selected as identifiable and to be (mis)identified as kaons. The latter quantities were measured in the data and led to corrections of up to 6%. These efficiencies are shown in fig. 8

Systematic uncertainties for this analysis were grouped into efficiency and fit-related categories. The dominant contributions to the efficiency category were the uncertainty in the track-finding efficiency (see above) and the uncertainties in particle identification efficiencies, for which the statistical errors on the data calibrations were used. The total uncertainties on the reconstruction efficiencies varied between 4–6% for the $K^{*0}$ and 6–11% for the $\phi$, depending on momentum

In the case of the $\phi$, fitting systematics were evaluated by varying the signal shape as in the $V^0$ analysis. In addition, fits were repeated with the center shifted by $\pm 1\sigma$ from the PDG value. The effect of background fluctuations was evaluated by taking the largest variation in the result over a set of fits done with the background shape parameters $c_i$ fixed to all combinations of their fitted values $\pm 1\sigma$. The total fitting uncertainties were 2–8%.

In the case of the $K^{*0}$, we considered the same variations, as well as variation of the signal width by $\pm 1\sigma$ from the PDG value and several variations of the resonant background. The misidentification scale factors were varied by $\pm 50\%$ for the $\pi\pi$ category and $\pm 15\%$ for the others in all 8 combinations, and the largest variation taken as a systematic error. The production rate of each resonance was varied by the error on the PDG value. The sizes of the $\rho$ and $\omega$ contributions were varied in all four combinations of $\pm 30\%$ and $\pm 10\%$, respectively, and the largest variation was taken as a systematic

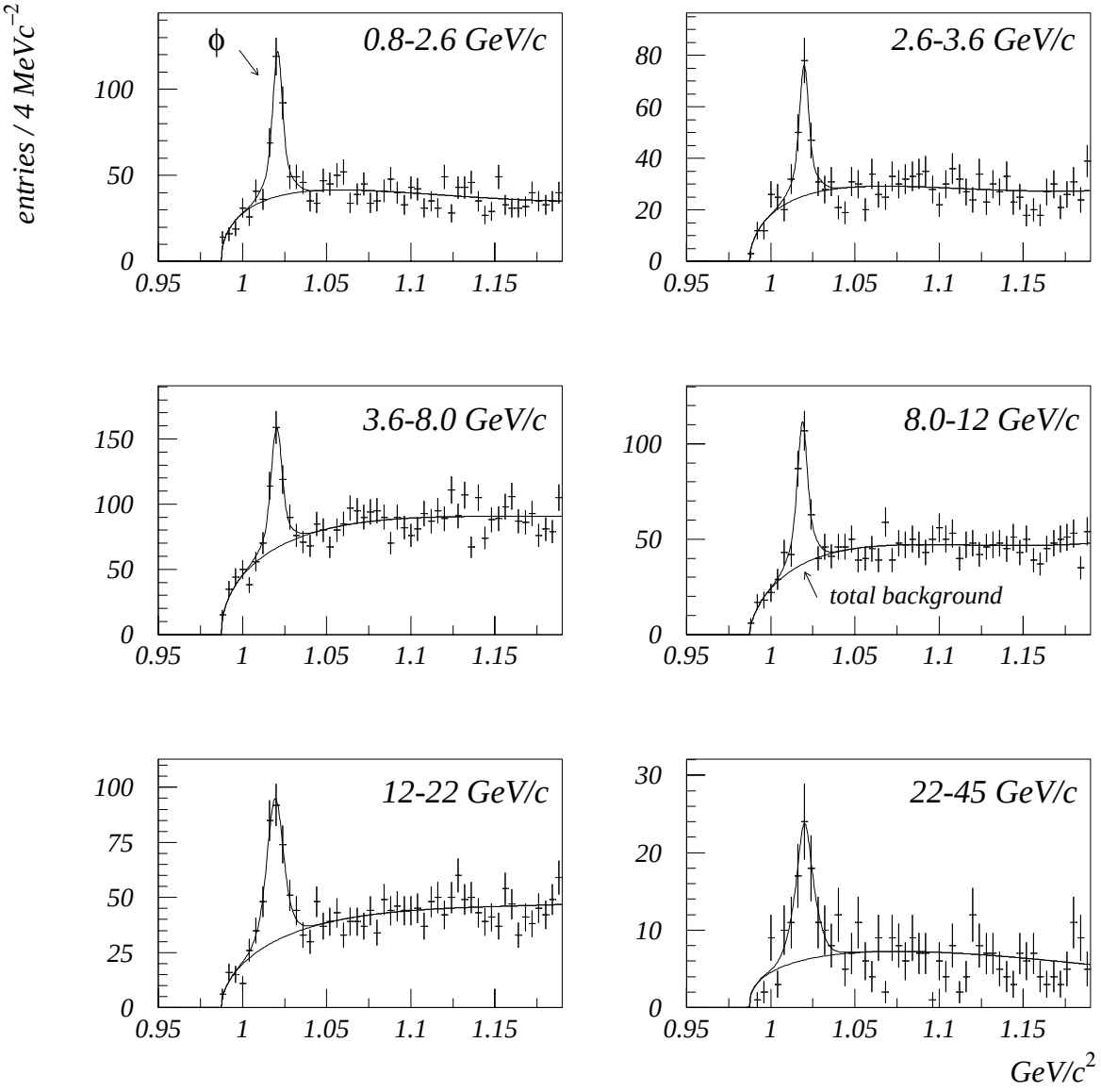


Figure 6: Distributions of invariant mass $m_{KK}$ for $\phi$ candidates in six scaled momentum bins. The points with error bars represent the data. The upper curves represent the results of the fits described in the text. The lower curves represent the fitted background component.

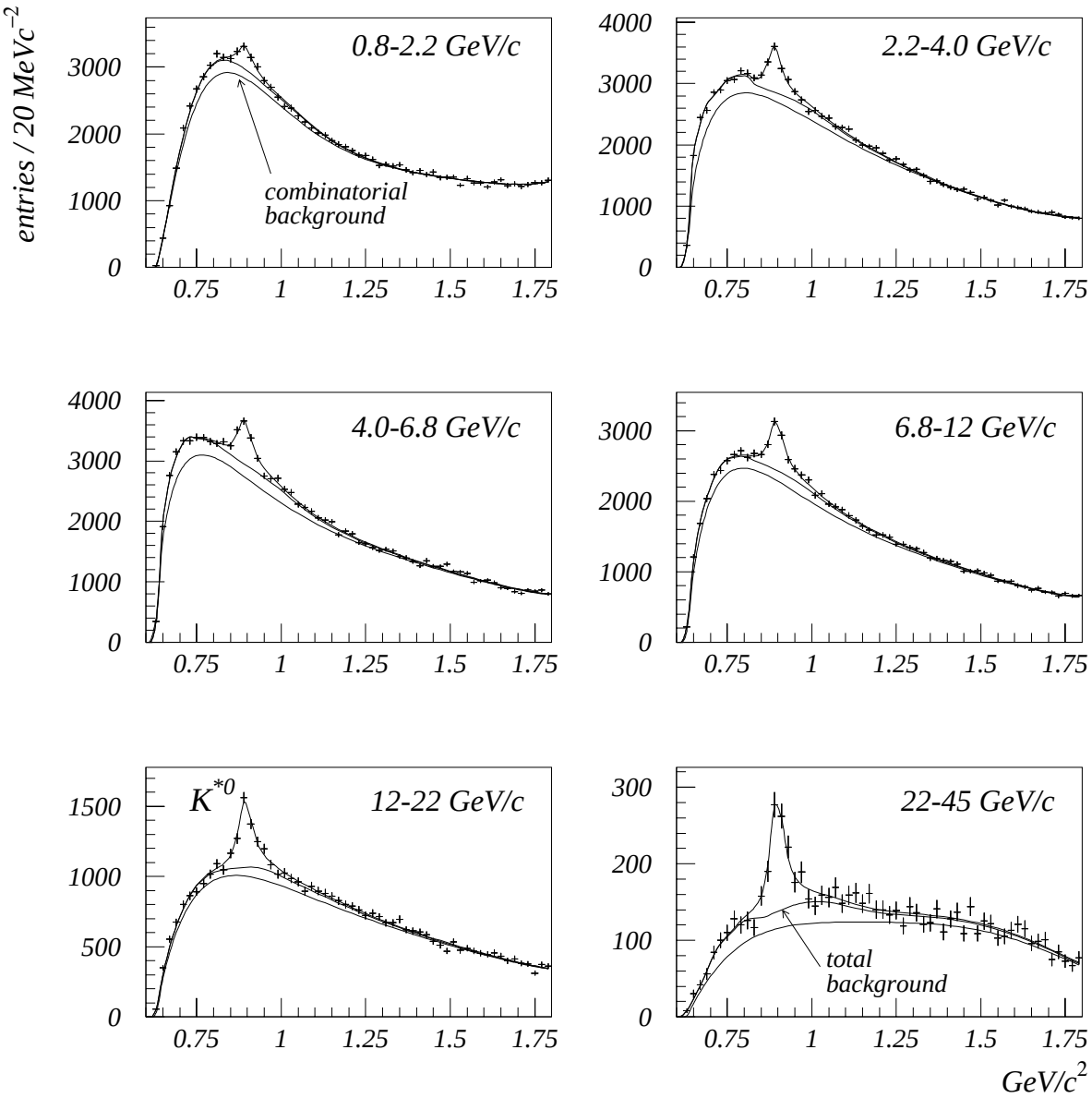


Figure 7: Distributions of invariant mass $m_{K\pi}$ for $K^{*0}/\bar{K}^{*0}$ candidates in six scaled momentum bins. The points with error bars represent the data. The upper curves represent the results of the fits described in the text. The middle and lower curves represent the fitted total background and combinatoric background components, respectively.

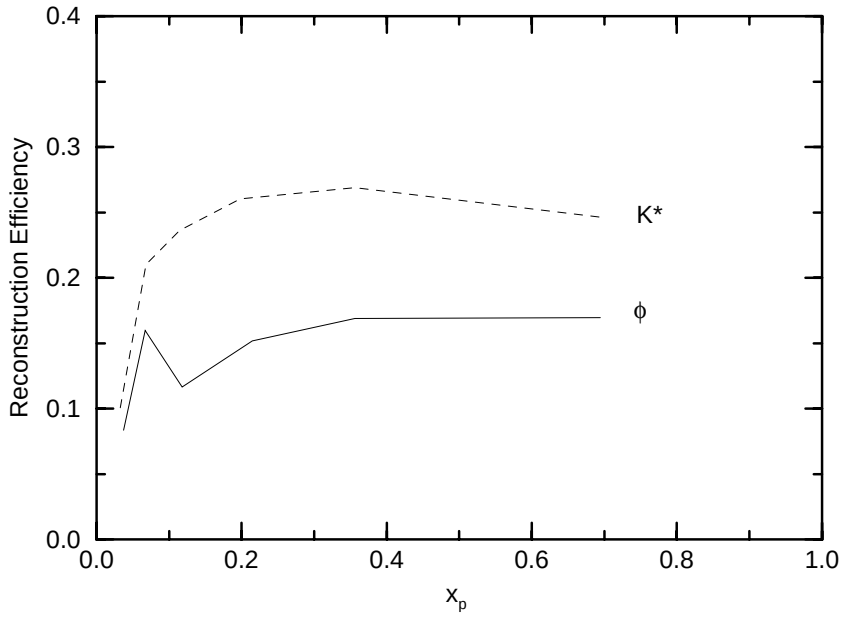


Figure 8: The simulated reconstruction efficiencies for $\phi$ (solid line) and $K^{*0}/\bar{K}^{*0}$ (dashed line). The charged decay branching ratios are included in the efficiency.

error. The shape of the $\rho$ contribution was changed by applying a scale factor linear in $m_{K\pi}$ that was unity at the $\rho$ peak and increased or decreased the contribution by 30% one half-width below the peak. The total fitting uncertainties are 2–6%.

# 7 Results for the Inclusive Event Sample

Figure 9 shows our measured differential cross sections per hadronic event of the seven hadron species as a function of scaled momentum $x_p$. At low $x_p$ pions are seen to dominate the particles produced in hadronic $Z^0$ decays. At $x_p \approx 0.03$, pseudoscalar kaons are produced at a rate about ten times lower, vector kaons are suppressed by a factor of $\sim$40, and the doubly strange vector $\phi$ by a factor of $\sim$500. The most commonly produced baryons, protons, are suppressed by a factor of $\sim$25, and the strange baryon $\Lambda^0$ by a factor of $\sim$75.

At high $x_p$, the pion and kaon production rates appear to be converging, as do the proton and lambda rates. This convergence could indicate reduced strangeness suppression at high momentum, or that production is becoming dominated by leading particles, such that kaons from $s\bar{s}$ events are as common as pions from $u\bar{u}$ and $d\bar{d}$ events.

Ratios of differential cross sections for various pairs of particles are shown in fig. 10. In the cases where the binning was different these ratios were obtained by fitting a curve to the denominator over a region around the $x_p$ value in question. The various strange-

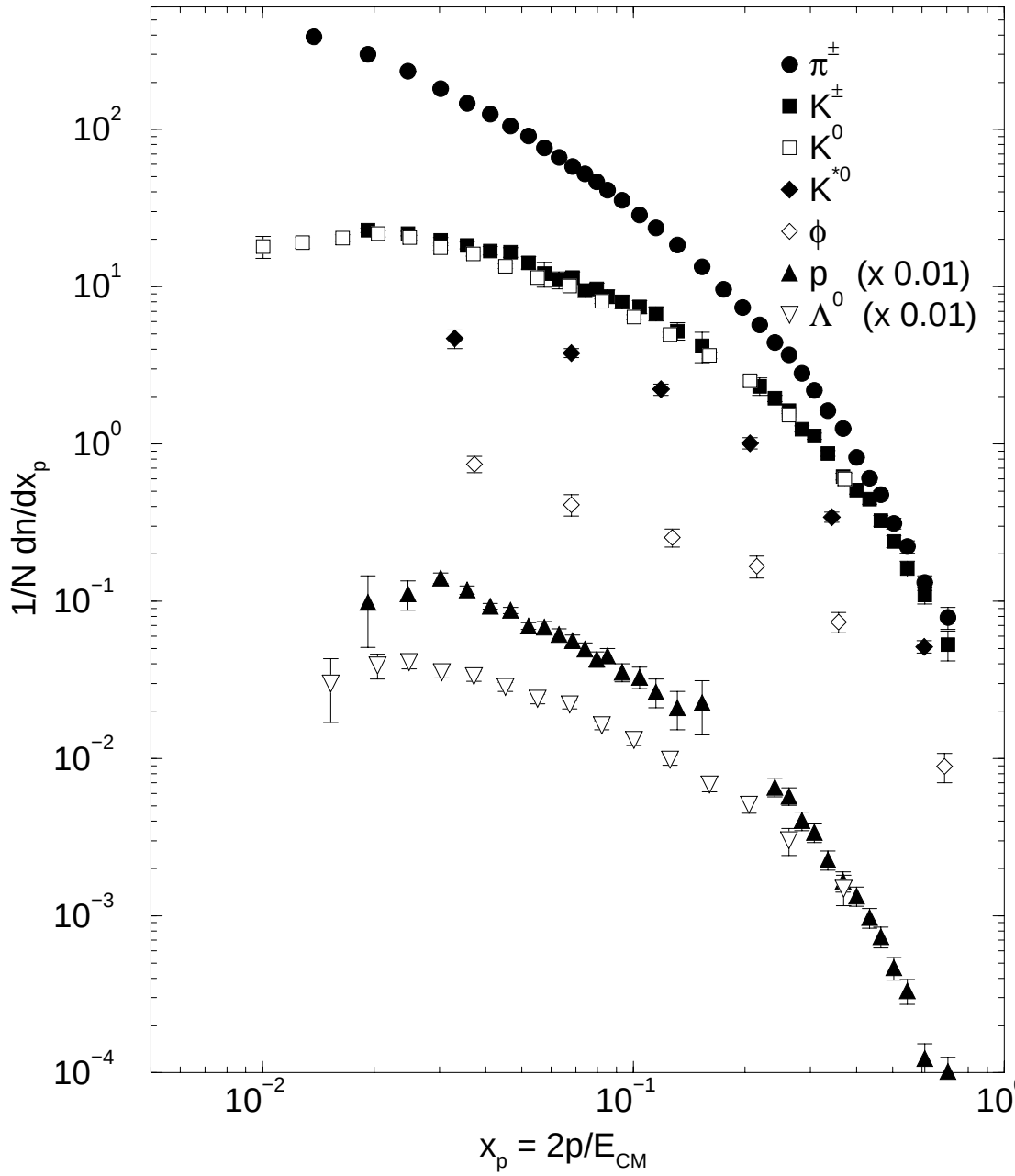


Figure 9: Production rates per event per unit scaled momentum, $x_p = 2p/E_{cm}$, for $\pi^{\pm}$ (dots), $K^{\pm}$ (squares), $K^0$ (open squares), $K^{*0}/\bar{K}^{*0}$ (diamonds), $\phi$ (open diamonds), $\mathrm{p}/\bar{\mathrm{p}}$ (triangles), and $\Lambda^0/\bar{\Lambda}^0$ (open triangles) in inclusive hadronic $Z^0$ decays. The $\mathrm{p}/\bar{\mathrm{p}}$ and $\Lambda^0/\bar{\Lambda}^0$ rates have been scaled by 0.01 for clarity. The errors are statistical and systematic added in quadrature. Overall normalization uncertainties of 1.7% (3.4%) on the charged (neutral) species are not included.

meson:pion ratios are well described by power laws over the measured $x_p$ range that steepen with increasing strange meson mass. The corresponding strange:nonstrange baryon ratio does not follow such a simple power law. The $K^0$:$K^\pm$ ratio is below unity over much of the range, indicating the presence of resonances that decay preferentially into charged kaons. Our measured $\phi$ rate accounts for only about 10% of this difference. The $K^{*0}$:$K^0$, $\phi$:$K^{*0}$, and $\Lambda^0$:$K$ ratios are roughly constant over the measured $x_p$ range, and the p:$\pi^\pm$ ratio is constant for $x_p > 0.2$.

In figs. 11 and 12 we compare our measured charged hadron fractions and neutral differential cross sections, respectively, with the predictions of the JETSET 7.4 [17] and HERWIG 5.7 [23] fragmentation models, using default parameters. The momentum dependence of all seven particle types is reproduced qualitatively by both models. The JETSET model proton and pion fractions are too high by 0.01–0.03 at large $x_p$, and the kaon fraction is too high at small $x_p$. The HERWIG model has a high pion fraction at intermediate $x_p$, and a prominent peak in the proton fraction at large $x_p$, compensated by a low kaon fraction, that is inconsistent with the data.

In the case of $K^0$, both models describe the data well at large $x_p$, but JETSET (HERWIG) overestimates the rate at small $x_p$ by as much as 35 (50)%. In the case of $\Lambda^0$, JETSET again describes the data well at large $x_p$, but falls 35% low at small $x_p$. HERWIG describes the data well at small $x_p$, but is high at large $x_p$ in a manner similar to that for the protons. In the case of $K^{*0}$ ($\phi$), the JETSET prediction is high by a factor of roughly 1.5 (2.0) across the entire $x_p$ range.

The JETSET predictions are also shown on fig. 10, showing a good qualitative description of the $x_p$ dependence of all measured ratios, and most of the normalization differences correspond to the features noted above. JETSET does predict a difference between charged and neutral kaon production, but it is smaller than that measured. Our data and conclusions about the predictions of fragmentation models are consistent with previous measurements from the LEP experiments [14, 15, 16, 24, 25, 26].

# 8 Flavor-Dependent Analysis

The analysis was repeated separately on the high-purity light- and $b$-quark event samples described in section 2, and on the remaining sample of events satisfying neither tag requirement, which we denote $c$-tag. In each momentum bin the measured differential cross sections $r_j^{meas}$ of each hadron species for these three samples, $j$ =light-tag, $c$-tag, $b$-tag, were unfolded by inverting the relations:

$$r_j^{meas} = \frac{\Sigma_i b_{ij} \epsilon_{ij} R_i r_i^{true}}{\Sigma_i \epsilon_{ij} R_i} \tag{3}$$

to yield true differential cross sections $r_i^{true}$ in events of the three flavor types, $i$ =1, 2, 3, corresponding to $Z^0 \to u\bar{u}, d\bar{d}, s\bar{s}$, $Z^0 \to c\bar{c}$ and $Z^0 \to b\bar{b}$. Here, $R_i$ is the fraction of hadronic $Z^0$ decays of flavor type $i$, taken from [22], $\epsilon_{ij}$ is the event tagging efficiency

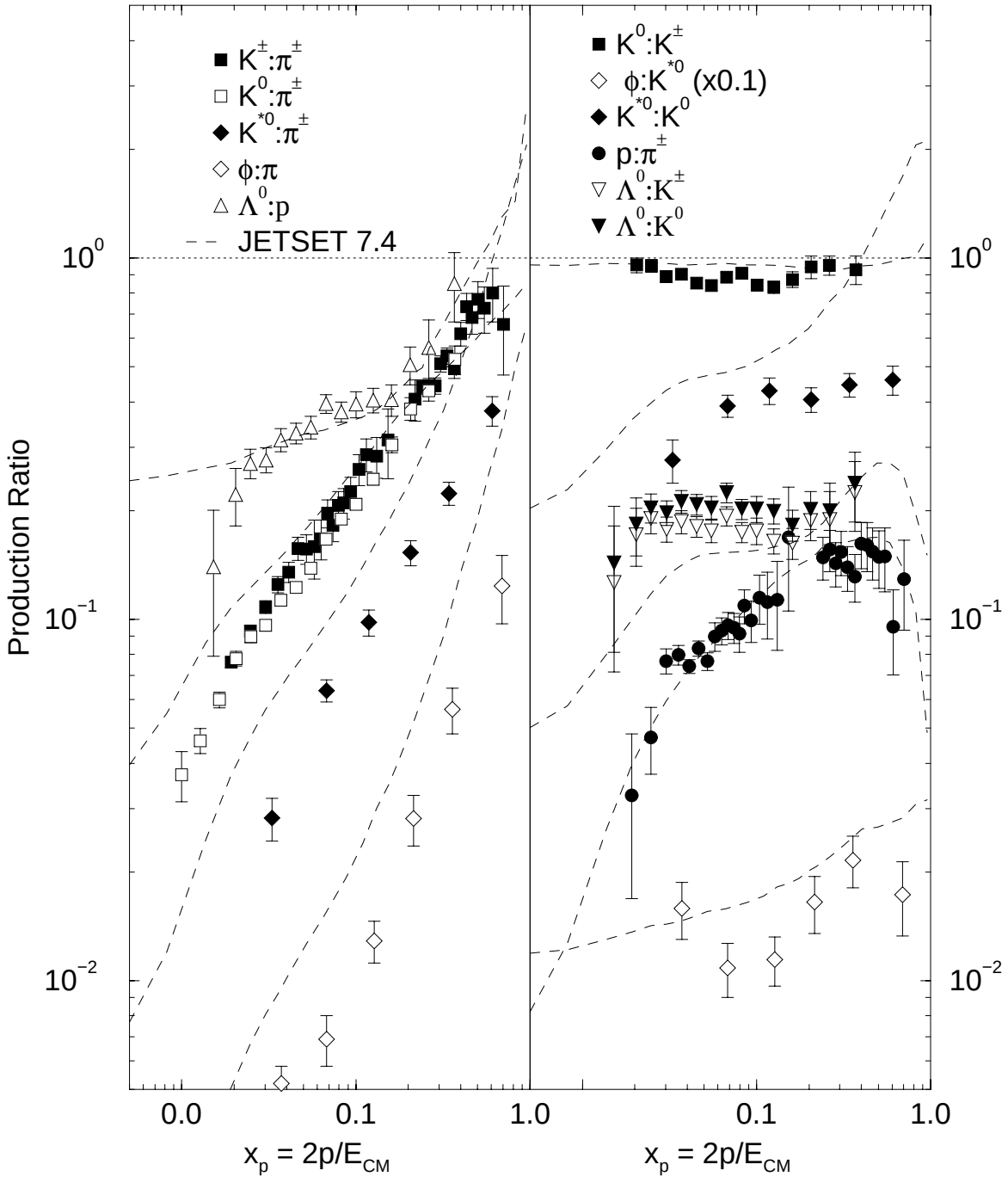


Figure 10: Production ratios for various pairs of identified hadrons in hadronic $Z^0$ decays, along with the predictions of the JETSET fragmentation model. In the cases of $K$:$\pi$ and $\Lambda$:$K$ the JETSET predictions for charged and neutral kaons have been averaged.

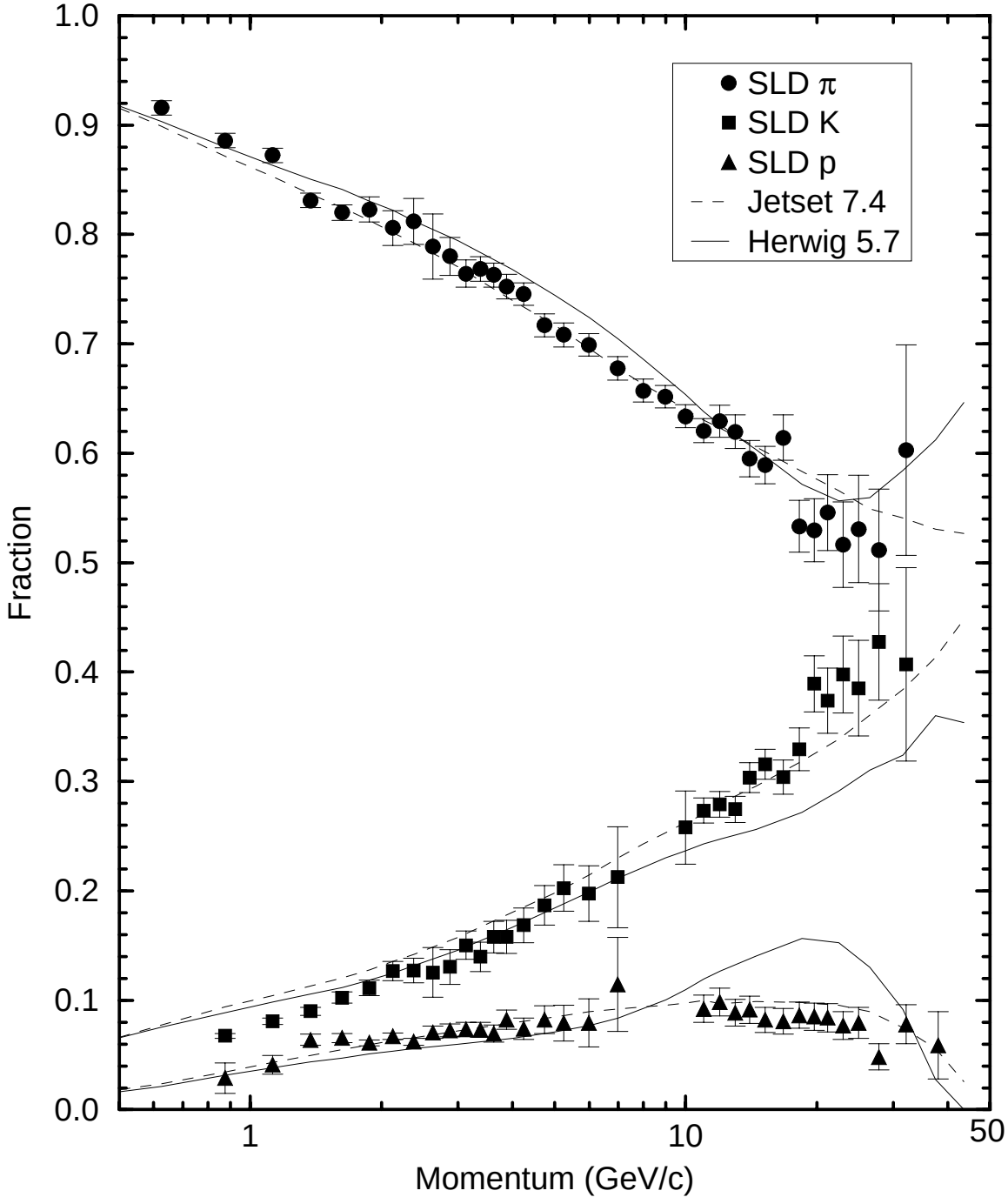


Figure 11: Comparison of our charged hadron fractions with predictions of two fragmentation models.

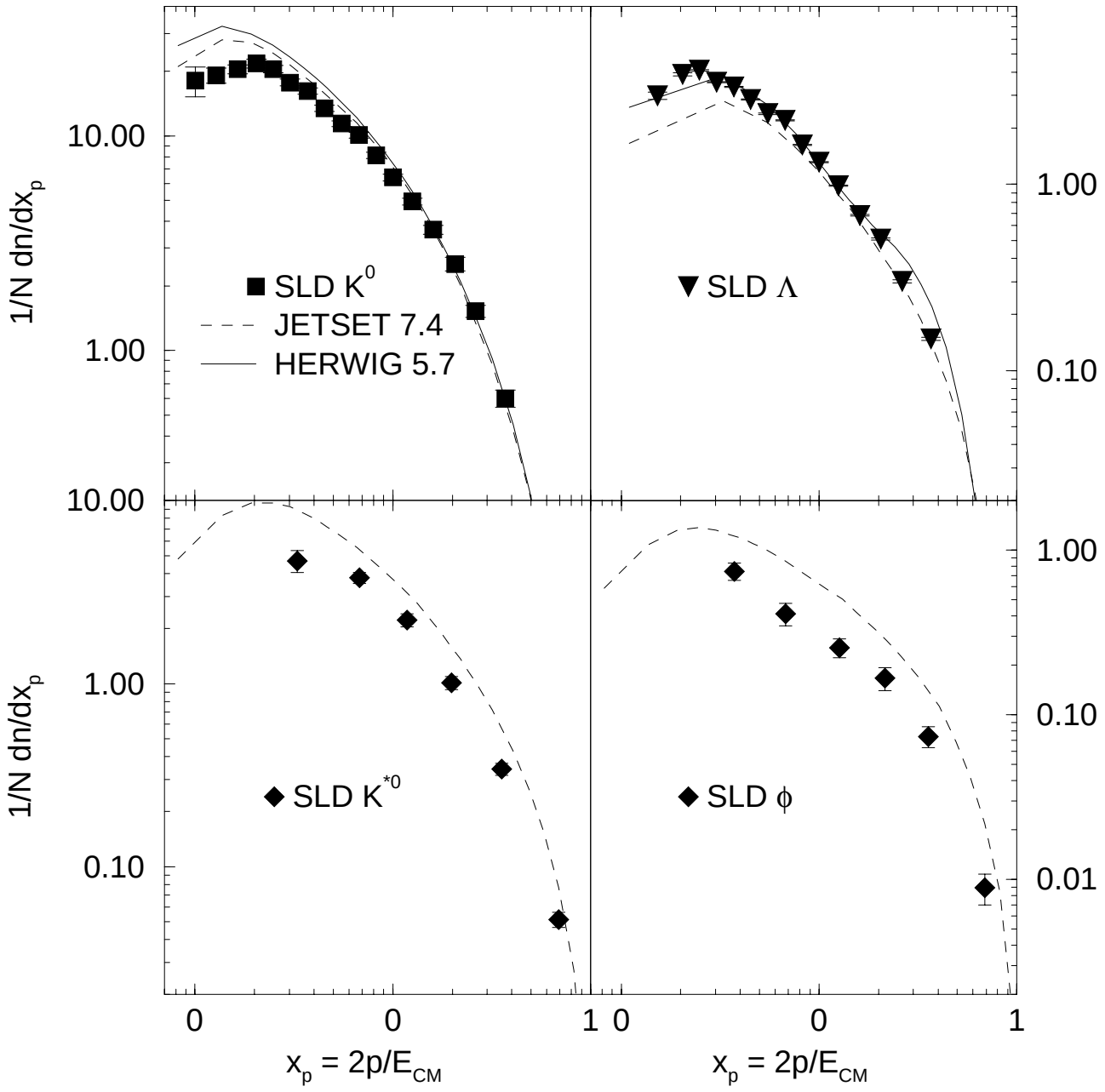


Figure 12: Comparison of our neutral particle differential cross sections with the predictions of two fragmentation models.

| | Efficiency for $Z^0 \rightarrow$ | | | Purity of $Z^0 \rightarrow$ | | |
|---|---|---|---|---|---|---|
| | $u\bar{u}, d\bar{d}, s\bar{s}$ | $c\bar{c}$ | $b\bar{b}$ | $u\bar{u}, d\bar{d}, s\bar{s}$ | $c\bar{c}$ | $b\bar{b}$ |
| light-tag | 0.845 | 0.438 | 0.075 | 0.849 | 0.124 | 0.027 |
| $c$-tag | 0.153 | 0.478 | 0.331 | 0.378 | 0.333 | 0.290 |
| $b$-tag | 0.002 | 0.084 | 0.594 | 0.009 | 0.100 | 0.891 |

Table 1: Tagging efficiencies for simulated events in the three flavor categories to be tagged as light, $c$ or $b$. The three rightmost columns indicate the composition of each simulated tagged sample assuming SM relative flavor production.

matrix, estimated from the simulation and listed in table 1, and $b_{ij}$ represents the momentum-dependent bias of tag $j$ toward selecting events of flavor $i$ that contain hadrons of the type in question. The diagonal bias values [13, 19, 21] are within a few percent of unity for the charged hadrons, $\phi$ and $K^{*0}$, reflecting a small multiplicity dependence of the flavor tags, and as much as 10% away from unity for the $V^0$, since some tracks from $V^0$ decays are included in the tagging track sample and have large impact parameter. The off-diagonal bias values are larger, but these have little effect on the unfolded results.

In fig. 13 we show differential cross sections for the seven hadron species in the light flavor sample. Qualitatively there is little difference between these and those for the inclusive sample (fig. 9) except for a slower falloff at high momentum. However, these differential cross sections are more relevant for comparison with QCD predictions based on the assumption of massless primary quark production, as well as for determining parameters in fragmentation models.

Comparison of each individual differential cross section with the two fragmentation models is shown in fig. 14, and the production ratios discussed in the previous section are shown in fig. 15. The same general features are seen as in figs 10–12, indicating that the presence of heavy flavors does not affect the qualitative features of the data, and that the deficiencies in the two fragmentation models are in the actual fragmentation simulation rather than in the modelling of heavy hadron production and decay. In particular, as in the inclusive flavor sample, the $K^0$:$K^{\pm}$ ratio is significantly below unity over the range $0.02 < x_p < 0.07$, indicating a cause in addition to decays of $D$- and $B$-hadrons.

In fig. 16 we show the ratios of production in $b$-flavor to light-flavor events for the seven species. The systematic errors on the particle identification largely cancel in these ratios, and the resulting errors are predominantly statistical. There is greater production of charged pions in $b$-flavor events at low momentum, with an approximately constant ratio for $0.02 < x_p < 0.07$. The production of both charged and neutral kaons is approximately equal in the two samples at $x_p = 0.02$, but the relative production in $b$-flavor events then increases with $x_p$, peaking at $x_p \approx 0.07$. The errors on the $K^{*0}$ and $\phi$

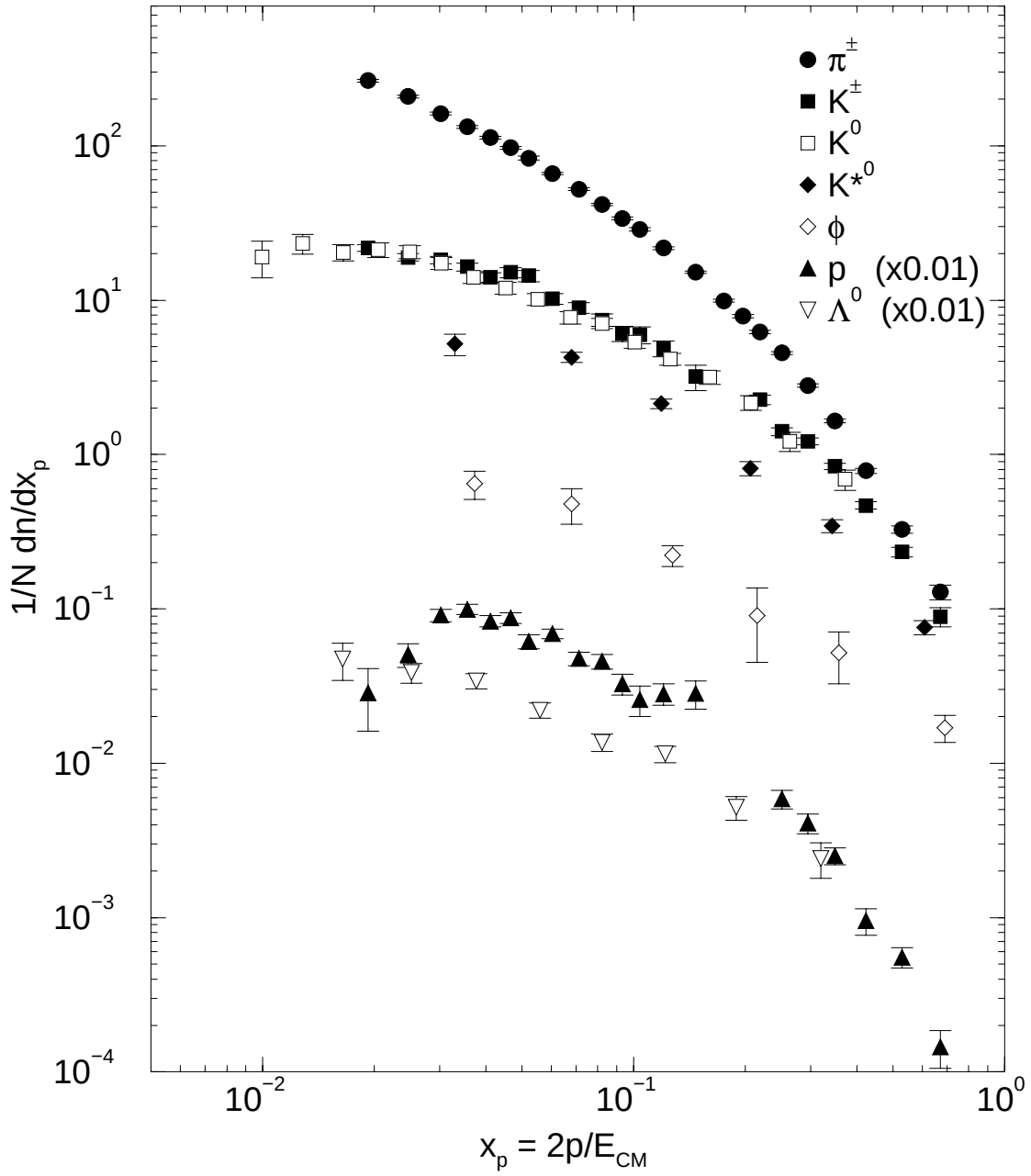


Figure 13: Differential cross section for the production of the seven hadron species in light-flavor events ($Z^0 \to u\bar{u}, d\bar{d}, s\bar{s}$)

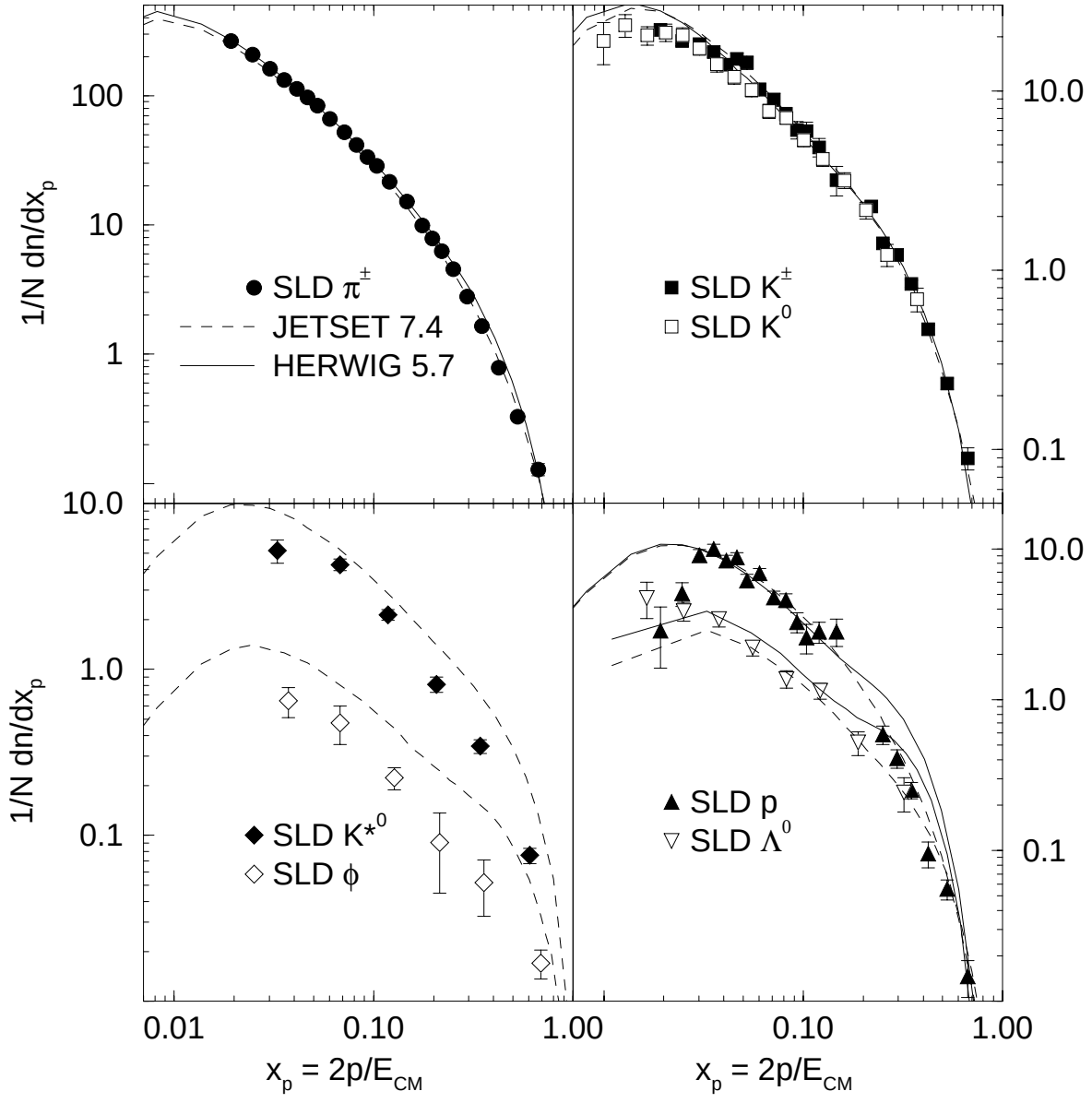


Figure 14: Comparison of our identified particle production rates in light-flavor events with the predictions of two fragmentation models.

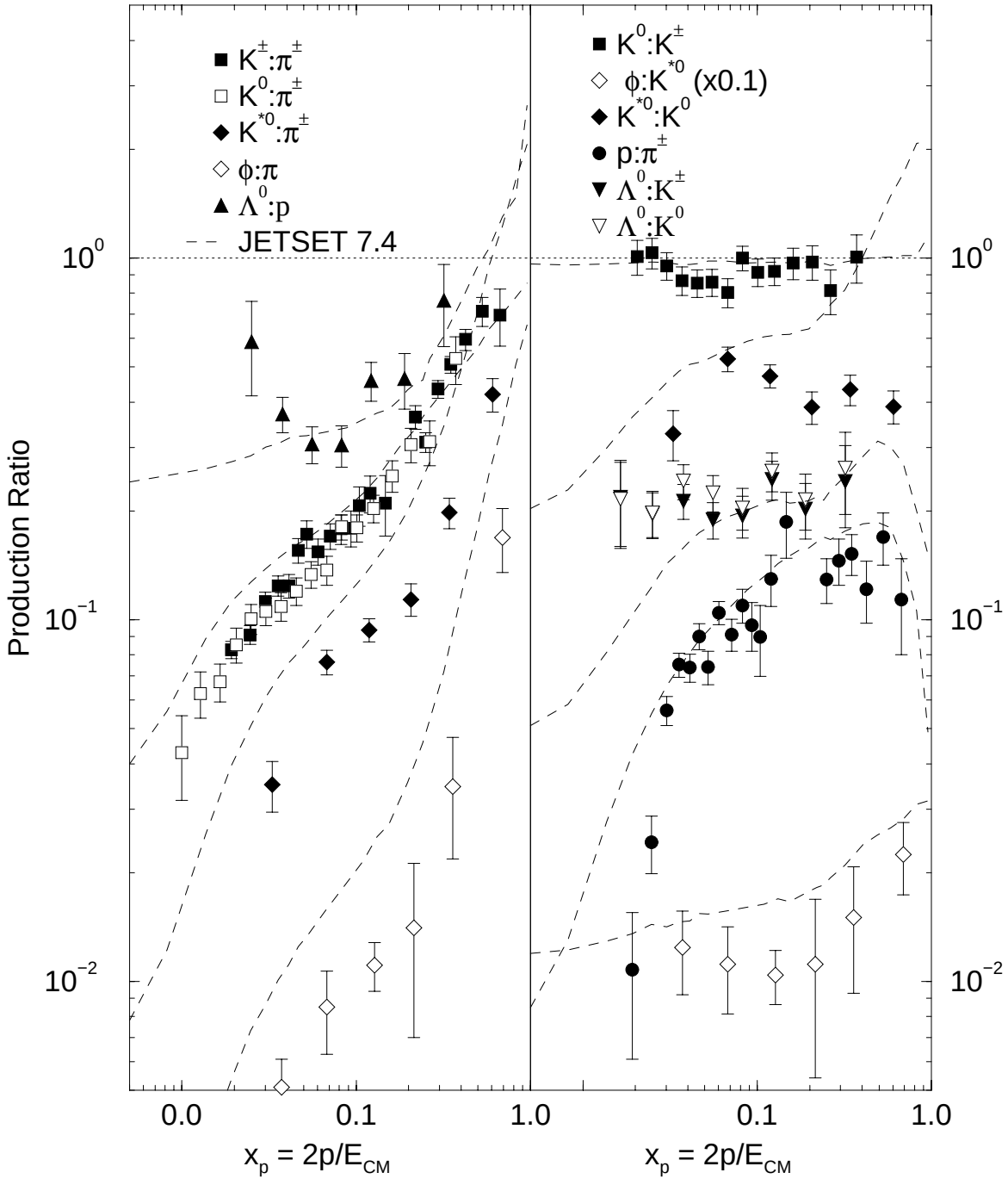


Figure 15: Production ratios in light-flavor events, along with the predictions of the JETSET fragmentation model. In the cases of $K{:}\pi$ and $\Lambda{:}K$ the JETSET predictions for charged and neutral kaons have been averaged.

ratios are large, but they are qualitatively similar to the kaon ratios, with an indication that the peak may be at a larger $x_p$ value. There is approximately equal production of baryons in $b$-flavor and light-flavor events below $x_p = 0.15$. For $x_p > 0.1$, production of all particle types falls faster with increasing momentum in $b$-flavor events. These features are consistent with expectations based on the known properties of $Z^0 \to b\bar{b}$ events, namely that a large fraction of the event energy is carried by the leading $B$- and $\bar{B}$-hadrons, which decay into a large number of lighter particles. Also shown in fig. 16 are the predictions of two fragmentation models, both of which reproduce these features qualitatively, although HERWIG overestimates the pion and kaon ratios by a large factor at low $x_p$.

In fig. 17 we show the corresponding ratios of production in $c$-flavor to light-flavor events for the seven species. The statistical errors are larger than for the $b$:light comparison and in some cases bins have been combined for clarity. Features qualitatively similar to those in the $b$:light comparison are observed. There is higher kaon production in $c$-flavor events than in light-flavor events at $x_p \sim 0.1$, reflecting the tendency of $c$-jets to produce a fairly hard charmed hadron whose decay products include a kaon carrying a large fraction of its momentum. There are fewer additional charged pions produced in $D$ decays than in $B$ decays, so that pion production is only slightly higher in $c$-flavor events at very small $x_p$. The pion $c$:light ratio starts to cut off at a larger value, $x_p \approx 0.3$, than the corresponding $b$:light ratio, attributable to the lower average decay multiplicity and softer fragmentation function of $D$ hadrons, and the kaon ratios are consistent with this cutoff point. The $c$:light ratios for vector particles and baryons are not precise enough to make any clear statements, but are consistent with unity at low $x_p$ and with the same cutoff point as the pions. Also shown in fig. 17 are the predictions of the two fragmentation models, both of which are consistent with the qualitative features of the data, although HERWIG overestimates the pion ratio at small $x_p$, as it did in the $b$:light case.

# 9 Comparison with MLLA QCD+LPHD Predictions

Calculations using the modified leading logarithm approximation (MLLA) predict that the distribution of the variable $\xi = \ln(1/x_p)$ for partons in a parton shower evolved down to a virtuality scale $Q_0$ should have a shape that is well approximated by a Gaussian distribution within $\sim$1 unit of the peak, and approximated by a slightly distorted Gaussian over a wider range. The ansatz of LPHD requires that the spectrum of directly produced hadrons have this same form, and that the position of the peak of the distribution for a given hadron species depend on the hadron mass and the c.m. energy.

We consider first the inclusive flavor event sample. As an example, fig. 18 shows

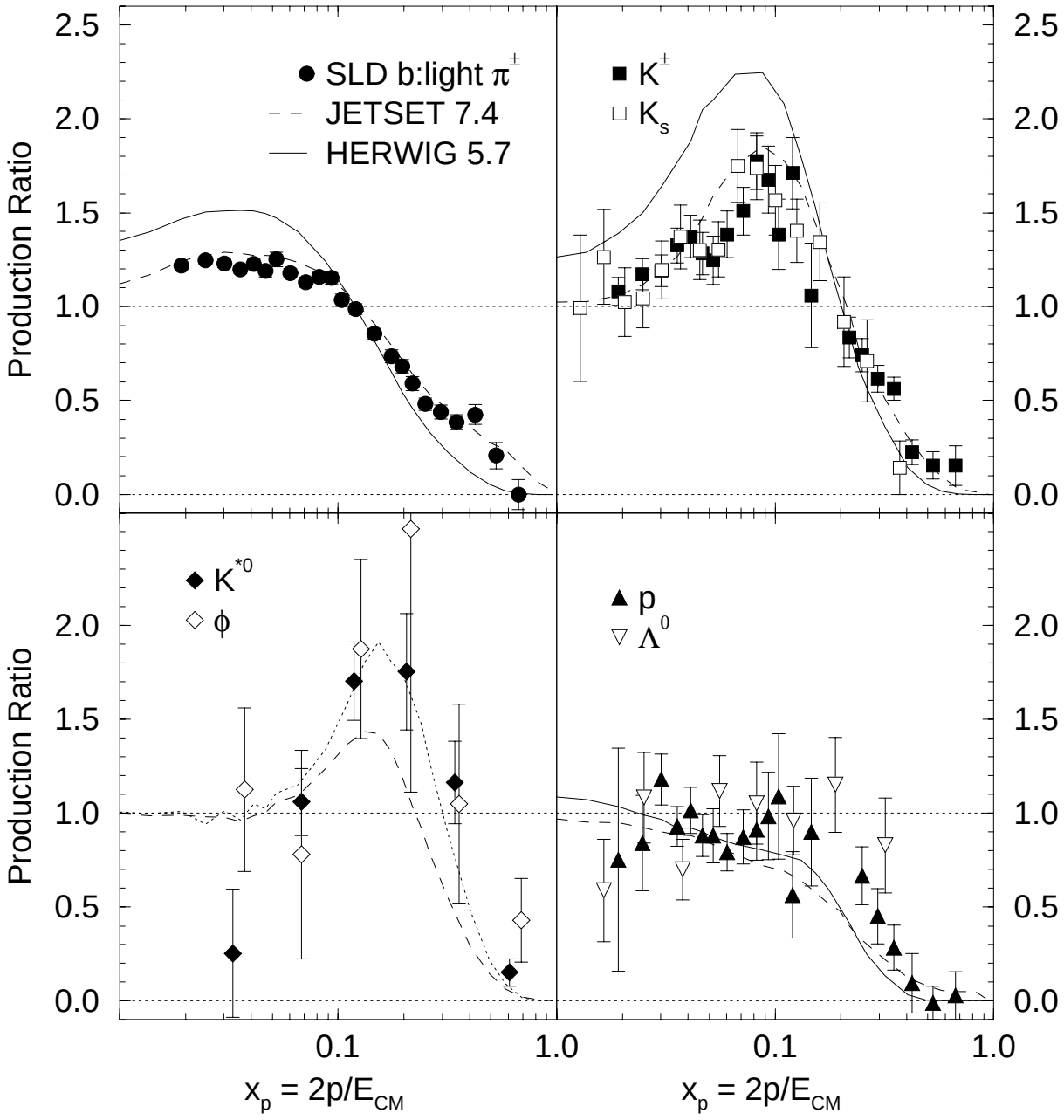


Figure 16: Ratios of production rates in $b$-flavor events to those in light-flavor events, along with the predictions of two fragmentation models. In the lower left plot, the dashed (dotted) line represents the JETSET prediction for $K^{*0}$ ($\phi$). In the right-hand plots, the predictions of a given model for the two particle types are very similar and have been averaged.

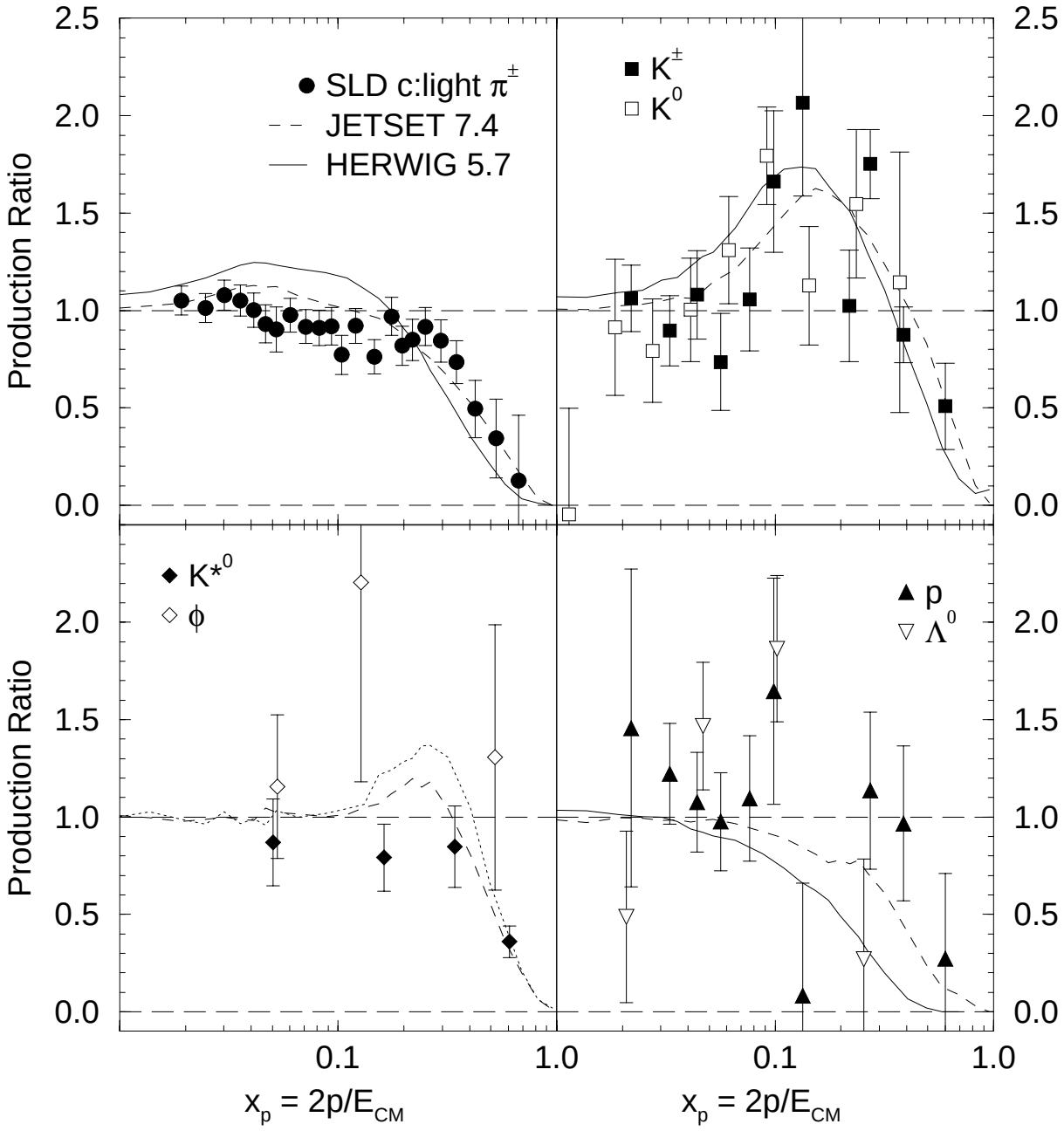


Figure 17: Ratios of production rates in $c$- and light-flavor events, along with the predictions of two fragmentation models. In the lower left plot, the dashed (dotted) line represents the JETSET prediction for $K^{*0}$ ($\phi$). In the right-hand plots, the predictions of a given model for the two particle types are very similar and have been averaged.

our measured differential cross section as a function of $\xi$ for the sharged kaons. Also shown are results of fits to a simple Gaussian (G), and a Gaussian including skewness and kurtosis terms (G++). In each case we maximized the range over which a good fit could be obtained, indicated by the dashed and solid curves, respectively, in fig. 18. The dotted and dot-dashed curves indicate the continuations of these functions. The G fit provides a good description of our data over a range of $\pm$ $\sim$1.3 units of $\xi$ around the peak position. The G++ function is able to describe the data over the full measured range, however the distortion terms are quite large. We conclude that the Gaussian prediction is consistent with our data in the peak region, but that our data are not sufficiently precise to make a meaningful test of the the additional terms in the G++ function. We note that this 5-parameter function is able to describe a wide range of distributions with similar shapes.

Similar results were obtained for the other particle types. Their $\xi$-distributions are shown in fig. 19 along with G fits. In each case the range over which an acceptable fit could be obtained was maximized and is indicated by the solid lines.

The peak position $\xi^*$ for each particle type was taken to be the mean value of the fitted Gaussian. Systematic errors were evaluated by varying the fit range and applying correlated experimental systematic errors. The peak positions are shown as a function of hadron mass in fig. 20, along with similar measurements from experiments at LEP. The pions peak at a higher $\xi$ value than the other particles, but otherwise there is no smooth mass-dependence, unless one hypothesizes that mesons and baryons lie on different trajectories in the $\xi^*$-mass plane.

A possible explanation for this absence of mass dependence is the fact that we have not measured primary fragmentation particles, rather a sample that includes decay products of an unknown mix of resonances as well as of heavy hadrons. This mix may affect peak positions differently for different particles types, although one might expect the largest effect to be for pions.

Therefore it is interesting to apply this test to our event samples of different primary flavors. In particular, we might expect to see a flavor dependence of the peak position, and possibly non-Gaussian shapes for heavy flavor events. Our measured $\xi$ distributions for the light-, c- and b-flavor events are shown in fig 21. There are clear differences between the different flavors, corresponding to those noted in the previous section, for example the distributions for pions and kaons in heavy-flavor events are narrower and higher than those in light-flavor events. However the peak positions are comparable. The simple Gaussian again provides an acceptable description of the distribution for all particles and flavors within $\pm$1 unit of the peak (not shown).

# 10 Leading Particle Effects

We extended [27] these studies to look for differences between particle and antiparticle production in quark (rather than antiquark) jets, in order to address the question of

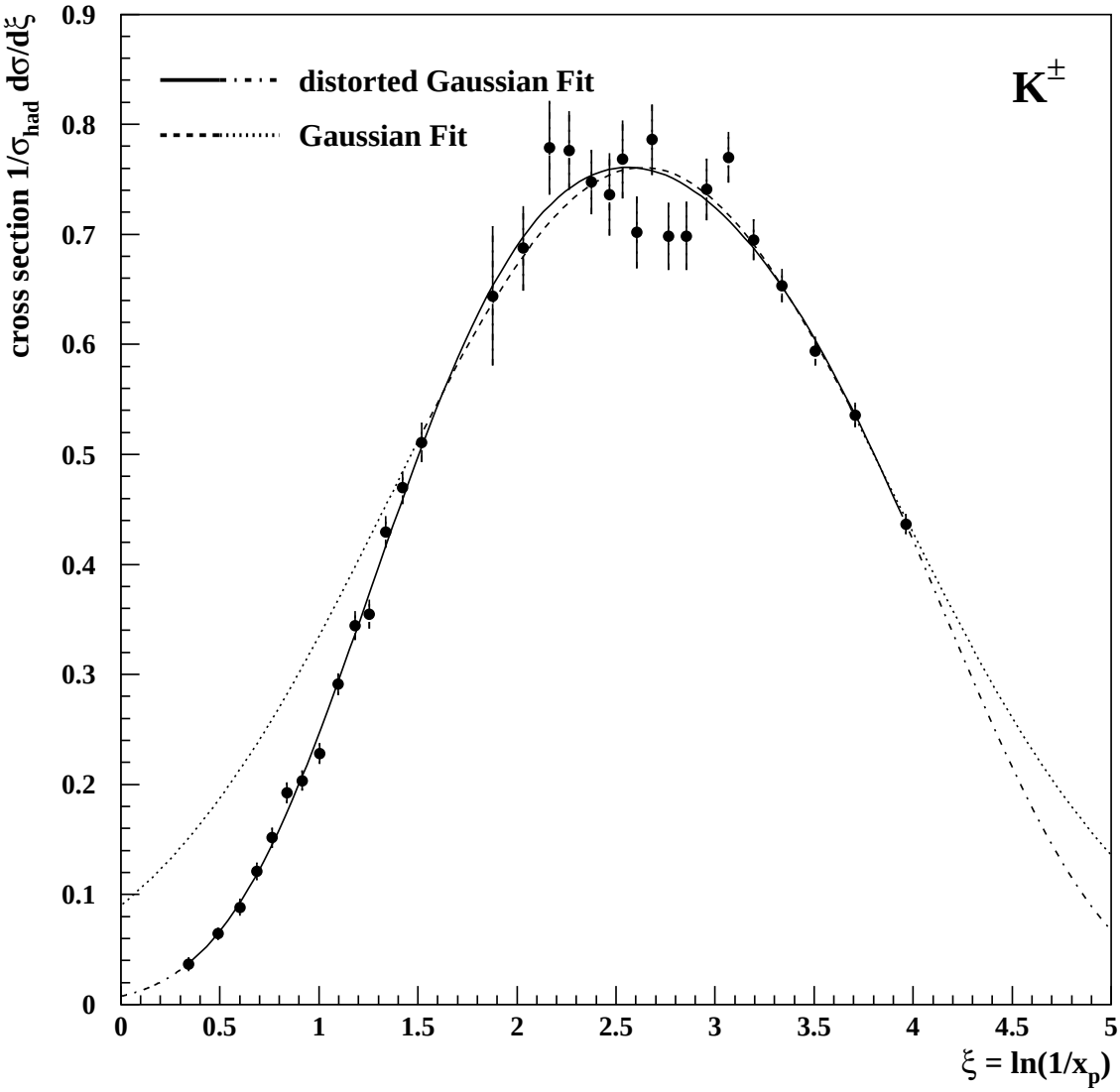


Figure 18: Distribution of $\xi = -\ln(x_p)$ for charged kaons in the flavor-inclusive sample along with the results of fits inspired by MLLA QCD (see text).

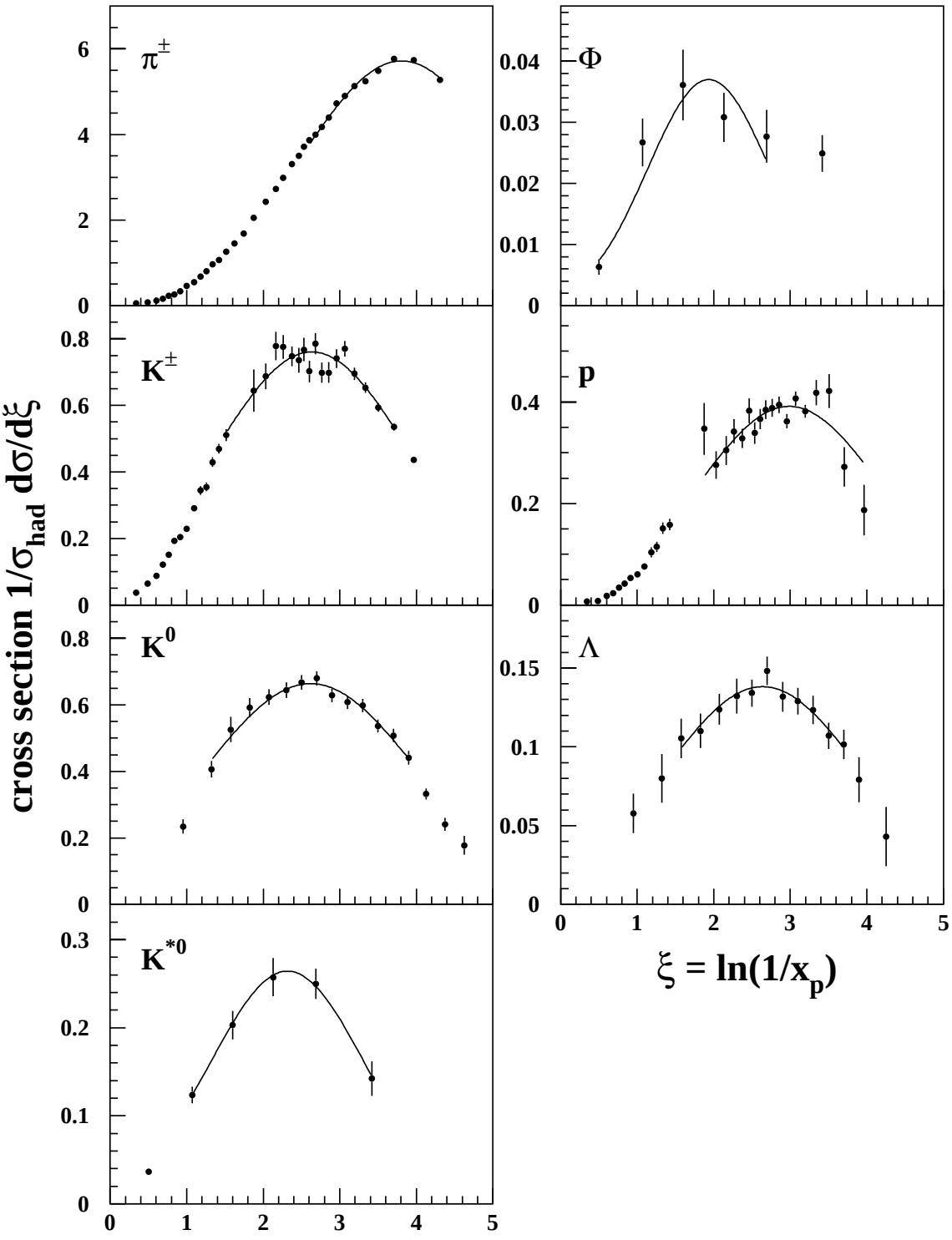


Figure 19: Distributions of $\xi$ for the seven hadron species in the flavor-inclusive sample along with the results of Gaussian fits (solid lines).

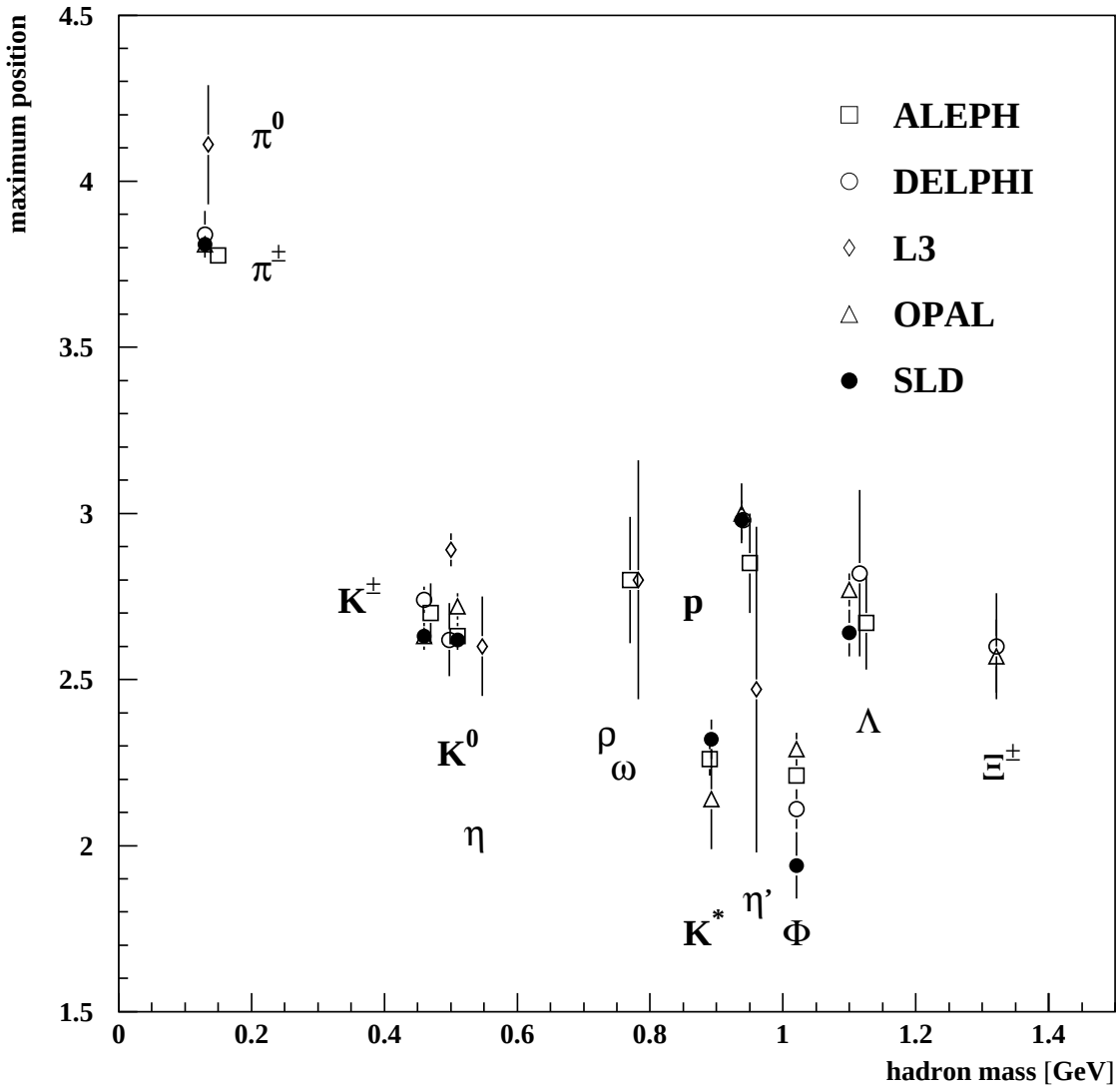


Figure 20: Peak positions $\xi^*$ from fits to the $\xi$ distributions in the flavor-inclusive sample, along with similar results from experiments at LEP.

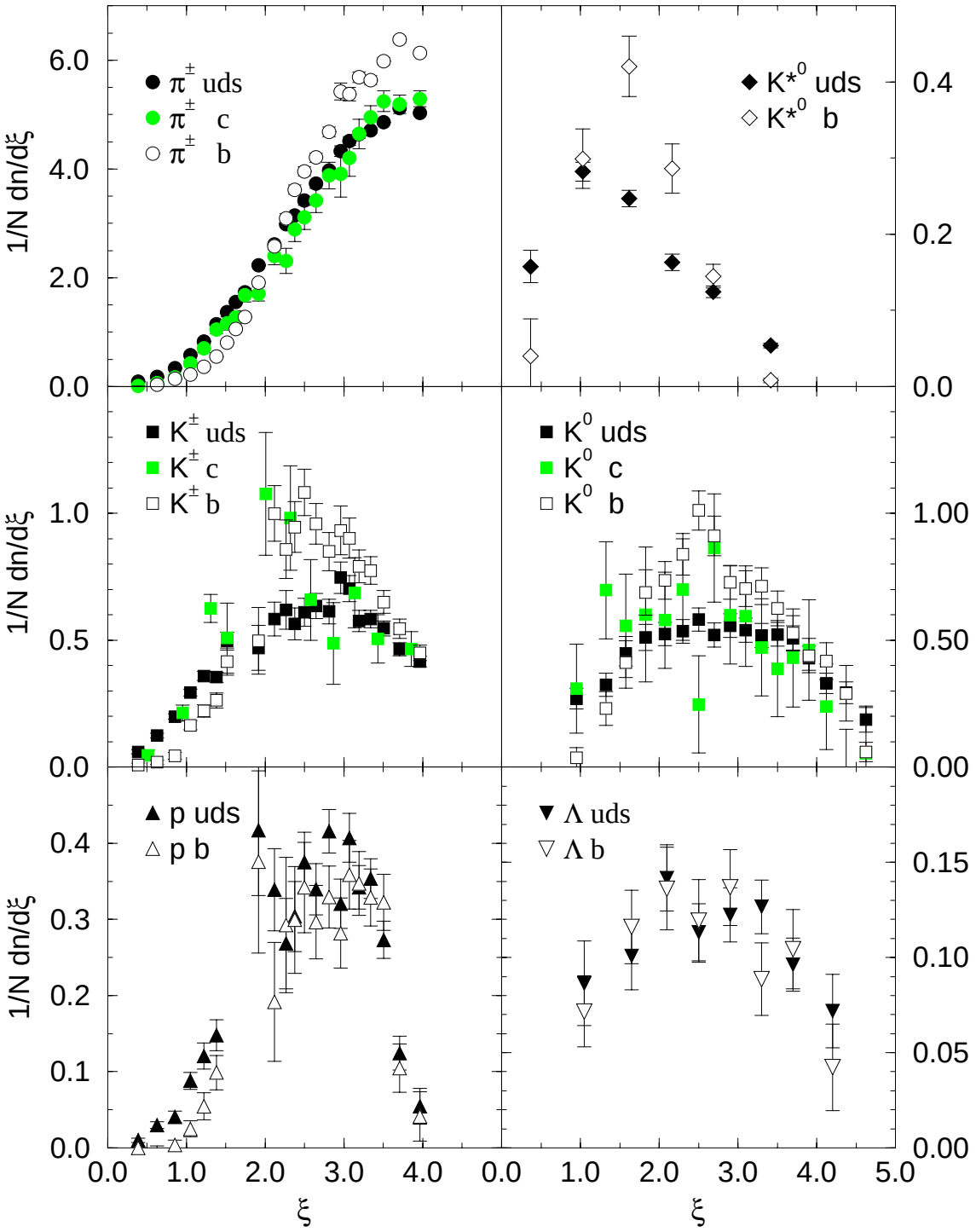


Figure 21: Distributions of $\xi$ for six hadron species for light-, $c$- and $b$-flavor events. Since the statistical errors are relatively large for the $c$-flavor sample, some points have been omitted and some bins combined for clarity.

whether e.g. a primary $u$-initiated jet contains more particles that contain a valence $u$-quark (e.g. $\pi^+$, $K^+$, $K^{*0}$, p, $\Lambda^0$) than particles that do not (e.g. $\pi^-$, $K^-$, $\bar{K}^{*0}$, $\bar{\mathrm{p}}$, $\bar{\Lambda}^0$). To this end we used the light quark- and antiquark-tagged hemispheres described in section 2.

We measured the production rates per light quark jet

$$R_h^q = \frac{1}{2N_{evts}} \frac{d}{dx_p} \left[ N(q \to h) + N(\bar{q} \to \bar{h}) \right], \quad (4)$$

$$R_{\bar{h}}^q = \frac{1}{2N_{evts}} \frac{d}{dx_p} \left[ N(q \to \bar{h}) + N(\bar{q} \to h) \right], \quad (5)$$

where: $q$ and $\bar{q}$ represent light-flavor quark and antiquark jets respectively; $N_{evts}$ is the total number of events in the sample; $h$ represents any of the identified hadrons $\pi^-$, $K^-$, $\overline{K}^{*0}$, p, and $\Lambda$, and $\bar{h}$ indicates the corresponding antiparticle. Then, for example, $N(q \to h)$ is the number of hadrons of type $h$ in light quark jets.

The charged hadron fractions analysis was repeated separately on the positively and negatively charged tracks in each of the quark- and antiquark-tagged samples. Results for the positively charged tracks in the quark-tagged sample and the negatively-charged tracks in the antiquark-tagged sample were consistent, so these two samples were combined and labelled as positively charged hadrons from light quark jets, yielding measured values of $R^q_{\pi^+}$, $R^q_{K^+}$, and $R^q_{\mathrm{p}}$ in the tagged samples. The same procedure applied to the remaining tracks yielded $R^q_{\pi^-}$, $R^q_{K^-}$, and $R^q_{\bar{\mathrm{p}}}$. The neutral $K^{*0}$ and $\Lambda^0$ analyses were applied similarly to the quark- and antiquark-tagged samples to yield $R^q_{\overline{K}^{*0}}$, $R^q_{K^{*0}}$, $R^q_{\Lambda}$ and $R^q_{\bar{\Lambda}}$.

It is essential to understand the contributions to these rates from heavy-flavor events, which are typically large in the momentum range we cover and show substantial differences between hadron and antihadron due to decay products of the heavy hadrons. This motivated our use of light-tagged events, and the residual heavy flavor contributions were estimated from the simulation to be typically 15% of the observed hadrons. This estimate was applied as a correction, yielding differential cross sections per light-quark-tagged jet. The effect of this correction on the results was negligible compared with the statistical errors.

For each hadron type, differential cross sections in light quark jets were then extracted by correcting for the light-tag bias and unfolding for the effective quark (vs. antiquark) purity. The purity was estimated from the simulation to be 0.76 for the $\Lambda^0/\bar{\Lambda}^0$ and 0.72 for the charged hadrons and $K^{*0}$, the latter value reflecting the cutoff in acceptance of the barrel CRID at $|\cos\theta| = 0.68$.

The measured differential cross sections per light quark jet are shown in fig 22. The systematic errors common to hadron and antihadron are not included, and the errors shown are predominantly statistical. Systematic uncertainties in the heavy-flavor background correction and the effective quark purity were considered and found to be smaller than the statistical errors.

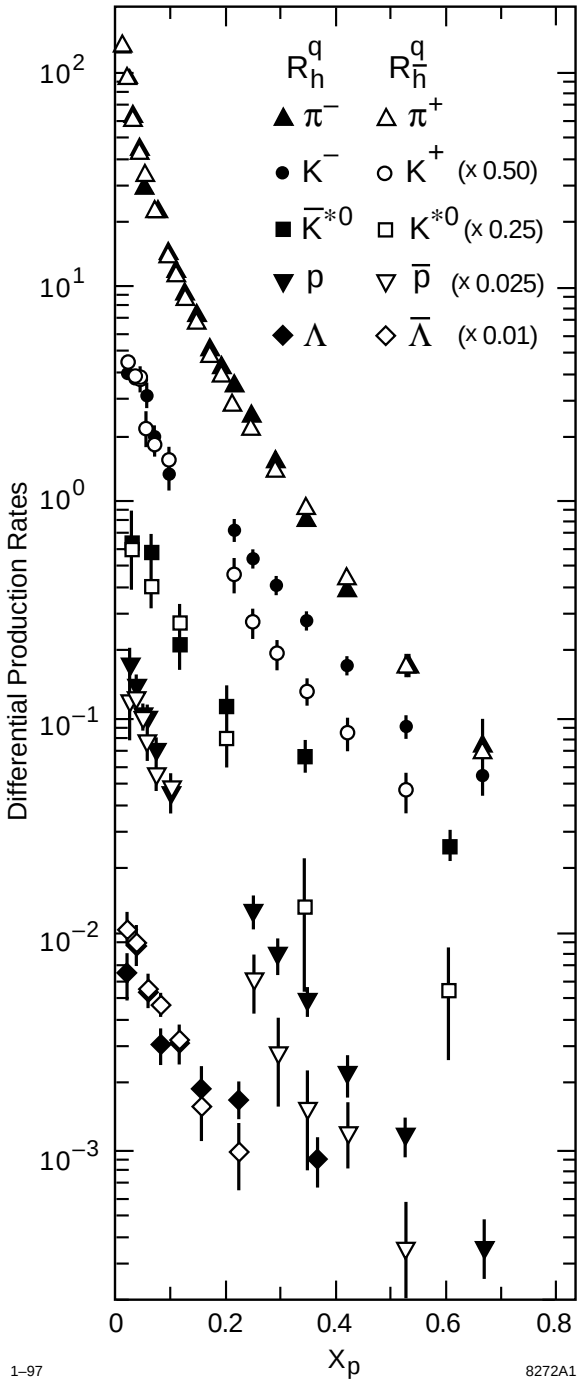


Figure 22: Momentum distributions of identified particles and their antiparticles in light quark ($u$, $d$, $s$) jets.

In all cases the hadron and antihadron differential cross sections are consistent at low $x_p$. For charged pions they are also consistent at high $x_p$, but for the other particles there are significant differences that appear to increase with increasing $x_p$. It is convenient to show these data in the form of the difference between hadron and antihadron differential cross sections normalized by the sum:

$$D_h = \frac{R_h^q - R_{\overline{h}}^q}{R_h^q + R_{\overline{h}}^q}, \tag{6}$$

The common systematic errors cancel explicitly in this variable. Results are shown in fig 23. A value of zero corresponds to equal production of hadron and antihadron, and the data are consistent with zero at low $x_p$. A value of +1 (–1) corresponds to complete dominance of (anti)hadrons $h$.

The baryon results are most straightforward to interpret. Since baryons contain valence quarks and not antiquarks, the excess of baryons over antibaryons in light quarks jets provides clear evidence for the production of leading protons at high scaled momentum. The data suggest that the effect increases with $x_p$.

The interpretation for the mesons is more complicated, since they contain one valence quark along with one antiquark. All down-type quarks are produced equally and with the same SM forward-backward asymmetry in $Z^0$ decays, so that if a leading neutral particle such as $K^{*0}$ $(d\bar{s})$ were produced equally in $d$ and $\bar{s}$ jets then our measured $D_{\overline{K}^{*0}}$ would be zero. For $x_p > 0.2$, we observe $D_{\overline{K}^{*0}} > 0$, indicating both substantial production of leading $K^{*0}/\overline{K}^{*0}$ mesons at high momentum, and a depletion of leading kaon production in $u\bar{u}$ and $d\bar{d}$ events relative to $s\bar{s}$ events.

In the case of charged mesons such as $\pi^-$ $(d\bar{u})$, the different production rates and forward-backward asymmetries of up- and down-type quarks cause a dilution of leading particle effects. At the $Z^0$, equal leading pion production in $u$- and $d$-jets would lead to a dilution factor of 0.27. For purposes of illustration, we have fitted a line to our $D_{\rm p}$ and $D_\Lambda$ points for $x_p > 0.2$ (dashed line in figs 23a and 23b), scaled it by the factor 0.27, and drawn it as the solid line on figs 23c and 23d.

Our measured $D_{\pi^-}$ are consistent with zero at all $x_p$, and significantly below this line at high $x_p$. This does not rule out leading primary pion production, but indicates nonleading production of pions must be relatively large. This could be due to a very soft leading pion momentum distribution and/or a large "background" contribution from decays of $\rho^0$, $K^*$, etc. Our measured $D_{K^-}$ are above the line for $x_p > 0.2$. As in the case of $D_{\overline{K}^{*0}}$, this indicates both production of leading charged kaons at high momentum, and a depletion of leading kaon production in $u\bar{u}$ and $d\bar{d}$ events relative to $s\bar{s}$ events.

Assuming these high-momentum kaons to be directly produced in the fragmentation process, this amounts to a direct observation of a suppression of $s\bar{s}$ production from the vacuum with respect to $u\bar{u}$ or $d\bar{d}$ production. In the case of $K^{*0}$ mesons it has been suggested [3] that this effect can be used to measure the "strangeness suppression parameter" $\gamma_s$, that is an important component of models of hadronization, see e.g.

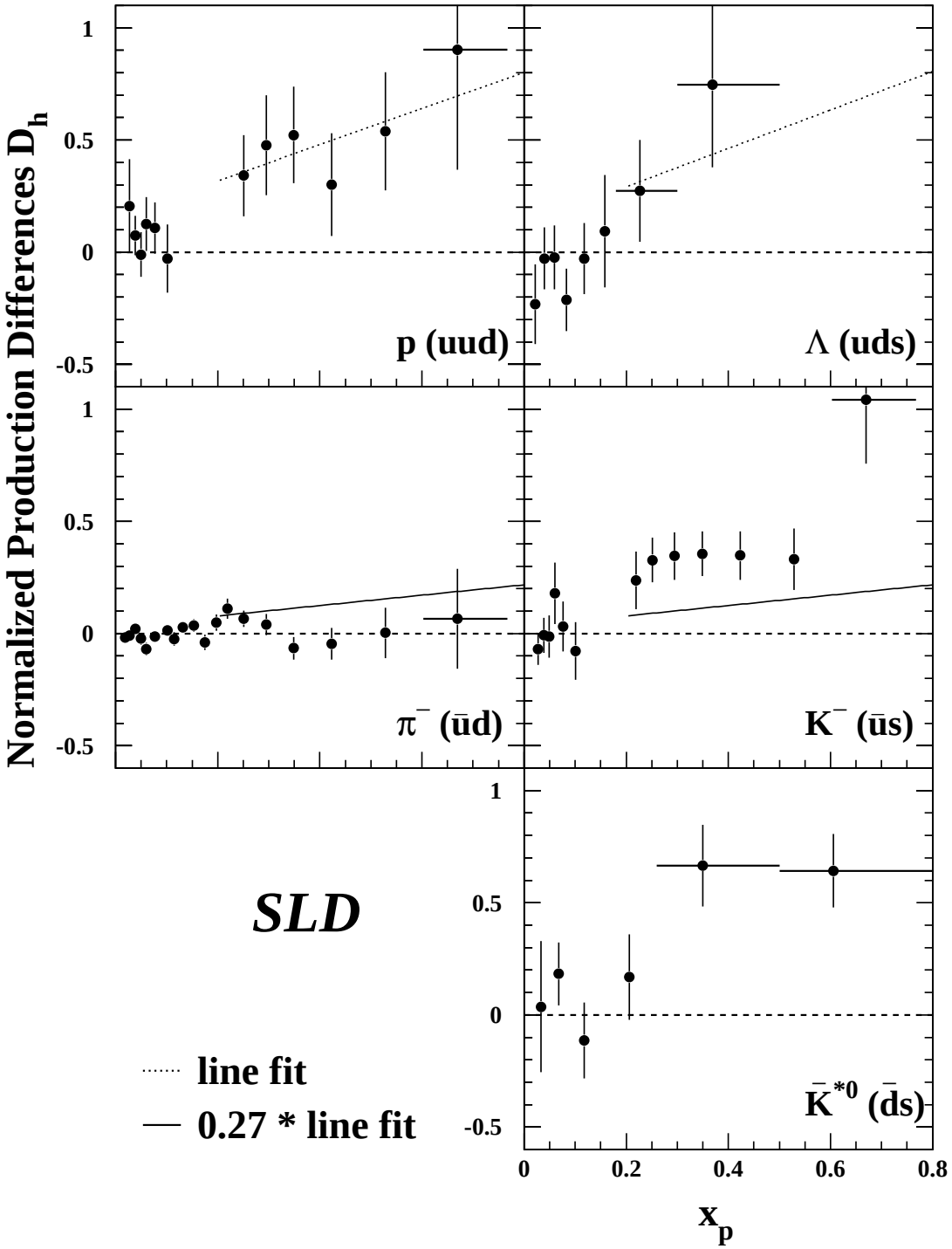


Figure 23: Normalized production differences between hadrons and their respective antihadrons in light quark jets. The dotted lines represent the results of a linear fit to the baryon data for $x_p > 0.2$, and the solid lines represent this fit scaled by the factor 0.27 (see text).

Ref. [17]. Assuming *all* $K^{*0}$ and $\overline{K}^{*0}$ in the range $x_p > 0.5$ to be leading, we calculate $\gamma_s = 0.26 \pm 0.12$, consistent with values [28] derived from inclusive measurements of the relative production rates of strange and non-strange, pseudoscalar and vector mesons.

# 11 Summary and Conclusions

Using the SLD Cherenkov Ring Imaging Detector we have made preliminary measurements of charged pion, kaon and proton, as well as neutral $K^{*0}$ and $\phi$ production over most of the momentum range in hadronic $Z^0$ decays. The production of $K^0$ and $\Lambda^0/\bar{\Lambda}^0$ was also studied. We find the predictions of the JETSET and HERWIG fragmentation models to be in qualitative agreement with our data. We find the predictions of MLLA QCD+LPHD to be consistent with our data near the maximum in the $\xi$ distribution, but do not observe a smooth mass-dependence of the peak position. These results are in agreement with those from previous experiments.

By isolating high-purity light- and $b$-flavor samples, we have measured hadron production in light-flavor events, as well as in $c$- and $b$-flavor events. We find substantial differences in particle production between light- and heavy-flavor events, with the latter producing more mesons overall, but far fewer at high momentum. These qualitative features are expected given the hard fragmentation and high average decay multiplicity of heavy hadrons. The shapes of the $\xi$ distributions also differ substantially between light- and heavy-flavor events, the latter having distributions that are higher and narrower. However the peak positions for the different flavors are quite similar, indicating that the presence of heavy flavors does not alter the mass-dependence of the peak position substantially.

The light-flavor sample is more suitable for testing predictions of QCD that assume massless quarks, as well as for testing fragmentation models. We find differences between fragmentation model predictions and our data similar to those found in the inclusive sample, indicating that the deficiencies lie in the simulation of fragmentation rather than in that of heavy hadron production and decay. In particular we find a significant difference between charged and neutral kaon production in light-flavor events, that is larger than that predicted by the fragmentation models and larger than can be explained by production and decay of $\phi$ mesons.

By isolating high-purity light-quark and light-antiquark samples, we have made the first comparison of hadron and antihadron production in light-quark jets in $e^+e^-$ annihilation. We observed an excess of $\Lambda$ over $\bar{\Lambda}$, and an excess of p over $\bar{\mathrm{p}}$. These differences increase with momentum, and provide direct evidence for the "leading particle" hypothesis that high momentum baryons are more likely to contain the primary quark. No such difference was observed between $\pi^-$ and $\pi^+$ production. For kaons, we observed a significant excess of high momentum $K^-$ over $K^+$, and $\overline{K}^{*0}$ over $K^{*0}$, indicating that a high momentum kaon is likely to contain a primary quark or antiquark from the $Z^0$ decay, and that leading kaons are produced predominantly in $s\bar{s}$ events

rather than $d\bar{d}$ or $u\bar{u}$ events. In the case of $K^{*0}$ these data provide a new direct measurement of the strangeness supression parameter in jet fragmentation at high scaled momentum, $\gamma_s = 0.26 \pm 0.12$.

# Acknowledgements

We thank the personnel of the SLAC accelerator department and the technical staffs of our collaborating institutions for their outstanding efforts on our behalf.

*This work was supported by Department of Energy contracts: DE-FG02-91ER40676 (BU), DE-FG03-91ER40618 (UCSB), DE-FG03-92ER40689 (UCSC), DE-FG03-93ER40788 (CSU), DE-FG02-91ER40672 (Colorado), DE-FG02-91ER40677 (Illinois), DE-AC03-76SF00098 (LBL), DE-FG02-92ER40715 (Massachusetts), DE-FC02-94ER40818 (MIT), DE-FG03-96ER40969 (Oregon), DE-AC03-76SF00515 (SLAC), DE-FG05-91ER40627 (Tennessee), DE-FG02-95ER40896 (Wisconsin), DE-FG02-92ER40704 (Yale); National Science Foundation grants: PHY-91-13428 (UCSC), PHY-89-21320 (Columbia), PHY-92-04239 (Cincinnati), PHY-95-10439 (Rutgers), PHY-88-19316 (Vanderbilt), PHY-92-03212 (Washington); The UK Particle Physics and Astronomy Research Council (Brunel and RAL); The Istituto Nazionale di Fisica Nucleare of Italy (Bologna, Ferrara, Frascati, Pisa, Padova, Perugia); The Japan-US Cooperative Research Project on High Energy Physics (Nagoya, Tohoku); The Korea Science and Engineering Foundation (Soongsil).

# **List of Authors

K. Abe,[19] K. Abe,[30] T. Akagi,[28] N.J. Allen,[4] W.W. Ash,[28]† D. Aston,[28] K.G. Baird,[24] C. Baltay,[34] H.R. Band,[33] M.B. Barakat,[34] G. Baranko,[9] O. Bardon,[15] T. L. Barklow,[28] G.L. Bashindzhagyan,[18] A.O. Bazarko,[10] R. Ben-David,[34] A.C. Benvenuti,[2] G.M. Bilei,[22] D. Bisello,[21] G. Blaylock,[16] J.R. Bogart,[28] B. Bolen,[17] T. Bolton,[10] G.R. Bower,[28] J.E. Brau,[20] M. Breidenbach,[28] W.M. Bugg,[29] D. Burke,[28] T.H. Burnett,[32] P.N. Burrows,[15] W. Busza,[15] A. Calcaterra,[12] D.O. Caldwell,[5] D. Calloway,[28] B. Camanzi,[11] M. Carpinelli,[23] R. Cassell,[28] R. Castaldi,[23][a] A. Castro,[21] M. Cavalli-Sforza,[6] A. Chou,[28] E. Church,[32] H.O. Cohn,[29] J.A. Coller,[3] V. Cook,[32] R. Cotton,[4] R.F. Cowan,[15] D.G. Coyne,[6] G. Crawford,[28] A. D'Oliveira,[7] C.J.S. Damerell,[25] M. Daoudi,[28] R. De Sangro,[12] R. Dell'Orso,[23] P.J. Dervan,[4] M. Dima,[8] D.N. Dong,[15] P.Y.C. Du,[29] R. Dubois,[28] B.I. Eisenstein,[13] R. Elia,[28] E. Etzion,[33] S. Fahey,[9] D. Falciai,[22] C. Fan,[9] J.P. Fernandez,[6] M.J. Fero,[15] R. Frey,[20] T. Gillman,[25] G. Gladding,[13] S. Gonzalez,[15] E.L. Hart,[29] J.L. Harton,[8] A. Hasan,[4] Y. Hasegawa,[30] K. Hasuko,[30] S. J. Hedges,[3]

S.S. Hertzbach,[16] M.D. Hildreth,[28] J. Huber,[20] M.E. Huffer,[28] E.W. Hughes,[28] H. Hwang,[20] Y. Iwasaki,[30] D.J. Jackson,[25] P. Jacques,[24] J. A. Jaros,[28] Z. Y. Jiang,[28] A.S. Johnson,[3] J.R. Johnson,[33] R.A. Johnson,[7] T. Junk,[28] R. Kajikawa,[19] M. Kalelkar,[24] H. J. Kang,[26] I. Karliner,[13] H. Kawahara,[28] H.W. Kendall,[15] Y. D. Kim,[26] M.E. King,[28] R. King,[28] R.R. Kofler,[16] N.M. Krishna,[9] R.S. Kroeger,[17] J.F. Labs,[28] M. Langston,[20] A. Lath,[15] J.A. Lauber,[9] D.W.G.S. Leith,[28] V. Lia,[15] M.X. Liu,[34] X. Liu,[6] M. Loreti,[21] A. Lu,[5] H.L. Lynch,[28] J. Ma,[32] G. Mancinelli,[24] S. Manly,[34] G. Mantovani,[22] T.W. Markiewicz,[28] T. Maruyama,[28] H. Masuda,[28] E. Mazzucato,[11] A.K. McKemey,[4] B.T. Meadows,[7] R. Messner,[28] P.M. Mockett,[32] K.C. Moffeit,[28] T.B. Moore,[34] D. Muller,[28] T. Nagamine,[28] S. Narita,[30] U. Nauenberg,[9] H. Neal,[28] M. Nussbaum,[7]† Y. Ohnishi,[19] Y. Oishi,[19] D. Onoprienko,[29] L.S. Osborne,[15] R.S. Panvini,[31] C.H. Park,[27] H. Park,[20] T.J. Pavel,[28] I. Peruzzi,[12][b] M. Piccolo,[12] L. Piemontese,[11] E. Pieroni,[23] K.T. Pitts,[20] R.J. Plano,[24] R. Prepost,[33] C.Y. Prescott,[28] G.D. Punkar,[28] J. Quigley,[15] B.N. Ratcliff,[28] T.W. Reeves,[31] J. Reidy,[17] P.L. Reinertsen,[6] P.E. Rensing,[28] L.S. Rochester,[28] P.C. Rowson,[10] J.J. Russell,[28] O.H. Saxton,[28] T. Schalk,[6] R.H. Schindler,[28] B.A. Schumm,[6] J. Schwiening,[28] S. Sen,[34] V.V. Serbo,[33] M.H. Shaevitz,[10] J.T. Shank,[3] G. Shapiro,[14] D.J. Sherden,[28] K.D. Shmakov,[29] C. Simopoulos,[28] N.B. Sinev,[20] S.R. Smith,[28] M.B. Smy,[8] J.A. Snyder,[34] H. Staengle,[8] P. Stamer,[24] H. Steiner,[14] R. Steiner,[1] M.G. Strauss,[16] D. Su,[28] F. Suekane,[30] A. Sugiyama,[19] S. Suzuki,[19] M. Swartz,[28] A. Szumilo,[32] T. Takahashi,[28] F.E. Taylor,[15] E. Torrence,[15] A.I. Trandafir,[16] J.D. Turk,[34] T. Usher,[28] J. Va'vra,[28] C. Vannini,[23] E. Vella,[28] J.P. Venuti,[31] R. Verdier,[15] P.G. Verdini,[23] D.L. Wagner,[9] S.R. Wagner,[28] A.P. Waite,[28] S.J. Watts,[4] A.W. Weidemann,[29] E.R. Weiss,[32] J.S. Whitaker,[3] S.L. White,[29] F.J. Wickens,[25] D.C. Williams,[15] S.H. Williams,[28] S. Willocq,[28] R.J. Wilson,[8] W.J. Wisniewski,[28] M. Woods,[28] G.B. Word,[24] J. Wyss,[21] R.K. Yamamoto,[15] J.M. Yamartino,[15] X. Yang,[20] J. Yashima,[30] S.J. Yellin,[5] C.C. Young,[28] H. Yuta,[30] G. Zapalac,[33] R.W. Zdarko,[28] and J. Zhou,[20]

[1] *Adelphi University, Garden City, New York 11530*
[2] *INFN Sezione di Bologna, I-40126 Bologna, Italy*
[3] *Boston University, Boston, Massachusetts 02215*
[4] *Brunel University, Uxbridge, Middlesex UB8 3PH, United Kingdom*
[5] *University of California at Santa Barbara, Santa Barbara, California 93106*
[6] *University of California at Santa Cruz, Santa Cruz, California 95064*
[7] *University of Cincinnati, Cincinnati, Ohio 45221*
[8] *Colorado State University, Fort Collins, Colorado 80523*
[9] *University of Colorado, Boulder, Colorado 80309*
[10] *Columbia University, New York, New York 10027*

[11] *INFN Sezione di Ferrara and Università di Ferrara, I-44100 Ferrara, Italy*
[12] *INFN Lab. Nazionali di Frascati, I-00044 Frascati, Italy*
[13] *University of Illinois, Urbana, Illinois 61801*
[14] *E.O. Lawrence Berkeley Laboratory, University of California, Berkeley, California 94720*
[15] *Massachusetts Institute of Technology, Cambridge, Massachusetts 02139*
[16] *University of Massachusetts, Amherst, Massachusetts 01003*
[17] *University of Mississippi, University, Mississippi 38677*
[18] *Moscow State University, Institute of Nuclear Physics 119899 Moscow, Russia*
[19] *Nagoya University, Chikusa-ku, Nagoya 464 Japan*
[20] *University of Oregon, Eugene, Oregon 97403*
[21] *INFN Sezione di Padova and Università di Padova, I-35100 Padova, Italy*
[22] *INFN Sezione di Perugia and Università di Perugia, I-06100 Perugia, Italy*
[23] *INFN Sezione di Pisa and Università di Pisa, I-56100 Pisa, Italy*
[24] *Rutgers University, Piscataway, New Jersey 08855*
[25] *Rutherford Appleton Laboratory, Chilton, Didcot, Oxon OX11 0QX United Kingdom*
[26] *Sogang University, Seoul, Korea*
[27] *Soongsil University, Seoul, Korea 156-743*
[28] *Stanford Linear Accelerator Center, Stanford University, Stanford, California 94309*
[29] *University of Tennessee, Knoxville, Tennessee 37996*
[30] *Tohoku University, Sendai 980 Japan*
[31] *Vanderbilt University, Nashville, Tennessee 37235*
[32] *University of Washington, Seattle, Washington 98195*
[33] *University of Wisconsin, Madison, Wisconsin 53706*
[34] *Yale University, New Haven, Connecticut 06511*
† *Deceased*
[a] *Also at the Università di Genova*
[b] *Also at the Università di Perugia*

# References

[1] T.I. Azimov, Y.L. Dokshitzer, V.A. Khoze and S.I. Troyan, Z. Phys. **C27** (1985) 65.

[2] See e.g. I.G. Knowles and G.D. Lafferty, CERN-PPE/97-040.

[3] G. D. Lafferty, Phys. Lett. **B353** (1995) 541.

[4] SLD Design Report, SLAC-Report 273, (1984).

[5] M.D. Hildreth *et al.*, Nucl. Inst. Meth. **A367** (1995) 111.

[6] C. J. S. Damerell *et al.*, Nucl. Inst. Meth. **A288** (1990) 236.

[7] K. Abe, *et al.*, Nucl. Inst. Meth. **A343** (1994) 74.

[8] SLD Collab., K. Abe *et al.*, Phys. Rev. Lett. **73** (1994) 25.

[9] S. Brandt *et al.*, Phys. Lett. **12** (1964) 57;
E. Farhi, Phys. Rev. Lett. **39** (1977) 1587.

[10] SLD Collab., K. Abe *et al.*, Phys. Rev. **D53** (1996) 1023.

[11] SLD Collab., K. Abe *et al.*, Phys. Rev. **D53** (1996) 2271.

[12] K. Abe, *et al.*, Nucl. Inst. and Meth. **A371** (1996) 195

[13] T.J. Pavel, Ph. D Thesis, Stanford University, January 1997; SLAC-Report-495.

[14] DELPHI Collab., P. Abreu *et al.*, Nucl. Phys. **B444** (1995) 3.

[15] OPAL Collab., P.D. Acton *et al.*, Z. Phys. **C63** (1994) 181.

[16] ALEPH Collab., D. Buskulic *et al.*, Z. Phys. **C66** (1995) 355.

[17] T. Sjöstrand, Comp. Phys. Comm. **82** (1994) 74.

[18] ALEPH Collab., D. Decamp *et al.*, Z. Phys. **C55** (1992) 209.

[19] K.G. Baird, Ph. D Thesis, Rutgers University, December 1995; SLAC-Report-95-483.

[20] SLD Collab., K. Abe, *et al.*, Phys. Rev. Lett. **72** (1994) 3145.

[21] M.O. Dima, Ph. D Thesis, Colorado State University, March 1997; SLAC-Report-505.

[22] Particle Data Group, Phys. Rev. **D54** (1996) 1.

[23] G. Marchesini *et al.*, Comp. Phys. Comm. **67** (1992) 465.

[24] DELPHI Collab., P. Abreu *et al.*, Z. Phys. **C65** (1995) 587;
Phys. Lett. **B318** (1993) 249; Z. Phys. **C73** (1996) 61.

[25] OPAL Collab., P.D. Acton *et al.*, Z. Phys. **C73** (1997) 569;
Z. Phys. **C67** (1995) 389; Z. Phys. **C68** (1995) 1.

[26] ALEPH Collab., D. Buskulic *et al.*, Z. Phys. **C64** (1994) 361;
Z. Phys. **C69** (1996) 379.

[27] SLD Collab., K. Abe *et al.*, Phys. Rev. Lett. **78** (1997) 3442.

[28] D.H. Saxon, *High Energy Electron-Positron Physics*, Eds. A. Ali and P. Söding, World Scientific (1988), p. 539.